

Author response to referee comments

We thank the reviewers for their valuable inputs that helped to improve the manuscript. The manuscript was modified according to the reviewers' advices. The detailed line-by-line responses (written in black) to each referee report (reports are written in *blue*), respectively, as well as a list of the largest changes in the manuscript are listed below. A new version of the manuscript is the final part of this document. All the (major) changes are highlighted in *green*.

Anonymous Referee #1

Received and published: 15 December 2019

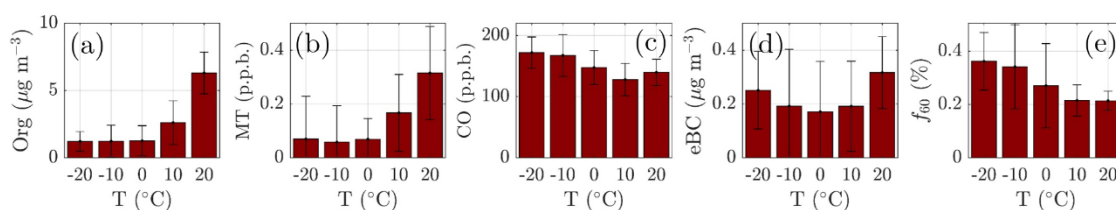
This manuscript reports an ACSM measurement study of sub-micron particles conducted at the SMEAR II atmospheric research station of Finland for a period of 7 years from 2012 to 2018. Discussions are made on temporal, diurnal and seasonal variations of PM₁ components, gaseous compounds including NO_x, SO₂, and monoterpene, and meteorological parameters such as temperature, solar radiation, wind speed and wind direction. Additionally, the influence of radiation, temperature and wind direction on major aerosol and gaseous species are examined. This is a worthy paper and a timely submission as it reports the longest online measurement data, to date, on sub-micron aerosol chemical composition in a boreal environment. It is suitable for publication on ACP and I recommend acceptance by the journal after the authors respond to the following comments.

While the title of the paper highlights aerosol chemical composition, the discussions focus more heavily on the inter- and intra-annual variations of PM₁ mass loading and meteorological conditions. The authors mention that more detailed discussions on organic aerosol factors determined from analysis of the ACSM mass spectra will be presented in a separate paper. While this decision is understandable considering the length of current manuscript, it is important that relevant discussions, such as biomass burning organic aerosols, are backed by measurement data such as variations in the ACSM f_{60} time series.

- The reviewer is right that f_{60} serves as a good marker for biomass burning. It has been for long associated with levoglucosan-like species that result from cellulose pyrolysis (Schneider et al., 2006; Alfara et al., 2007). The reviewer's statement is especially true in wintertime, when biomass burning organic aerosol (BBOA) is still fresh upon arrival to SMEAR II. The figures below (Figures AR.1&AR.3) clearly show how f_{60} is making up a larger fraction of the organic aerosol in winter. As the summertime BBOA emissions occur mostly faraway (wild fires rarely occur in Finland), BBOA has already photochemically transformed into oxidised organic aerosol (OOA) before reaching SMEAR II, and f_{60} has decreased to Northern hemispheric background levels ($f_{60} < \sim 0.03$; Cubison et al., 2011). Thus, f_{60} is necessarily not a good marker for summertime OA origins, but rather for *fresh* BBOA. Hence, we originally chose eBC and CO as better (~inert) markers for summertime biomass burning influence. The rapid (in order of several hours) photochemical aging of BBOA has been a topic of earlier chamber (Grieshop et al., 2009; Jimenez et al., 2009; Cubison et al., 2011) and ambient studies (DeCarlo et al., 2010; Cubison et al., 2011).

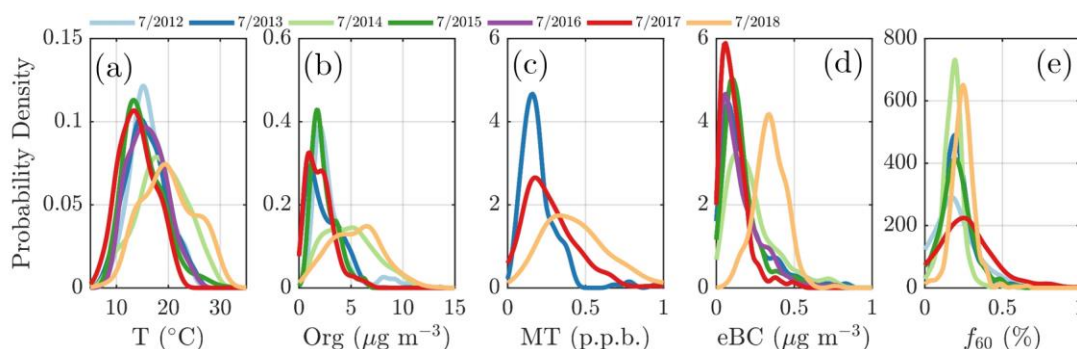
Manuscript modifications:

- We have added sub-panels to Figures 5&6 (Figures 5e&6e) in the manuscript to include f_{60} data. The revised figures are presented below as Figure AR.1 and Figure AR.2. We also added information regarding the f_{60} seasonal behaviour in form of Figure AR.3 in *Appendix A: Supporting figures* (Figure A.4 in the manuscript). Note the minor change in Figure 5 representation, as we wanted to include error bars (standard deviation) in the figure.



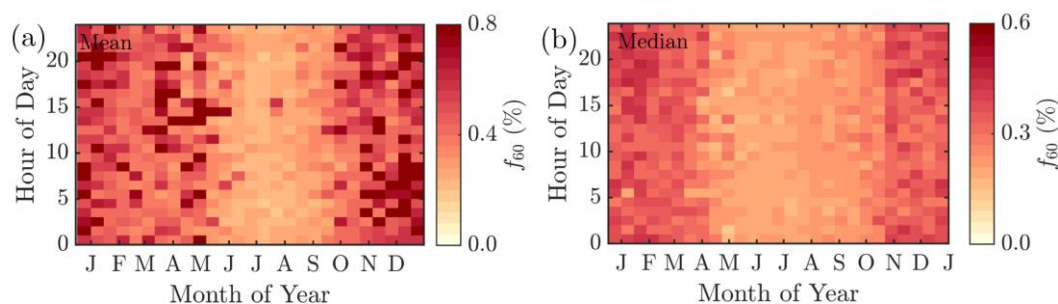
45
46
47
48
49

Figure AR.1 The daily mean organic aerosol (Org, panel a), monoterpene (MT, panel b), carbon monoxide (CO, panel c), equivalent black carbon (eBC, panel d) concentrations, and the fraction of the ACSM Org-signal made up by levoglucosan-like species (f_{60} , panel e) recorded under different ambient temperatures. The values recorded assigned into 10 °C wide bins based on the daily ambient temperature mean. The marker error bars show the standard deviation of the values in each bin.



50
51
52
53
54
55
56
57
58
59

Figure AR.2 Non-parametric probability densities (Kernel distributions) of temperature (panel a), organic aerosol (panel b), monoterpenes (panel c), equivalent black carbon (panel d) concentrations, and the fraction of the ACSM Org-signal made up by levoglucosan-like species (f_{60} ; panel e) during individual Julys across the measurement period (2012–2018). The data availability for eBC was one week in July 2018. The x-axes represent the T, Org, MT and eBC values recorded, respectively and the y-axes the non-parametric probability densities. Briefly, the Kernel distributions are similar to smoothed histograms of the measurement data. This visualisation was chosen to avoid assumptions of the nature of distribution that might hide important features of the measurement data if presented with normal distributions, for instance.



60
61
62
63
64
65
66
67
68

Figure AR.3 The mean (a-panel) and median (b-panel) f_{60} (the fraction of m/Q 60 Th signal of the total OA signal) values derived from the ACSM measurements (2012–2018 at SMEAR II). The x-axes represent the time of the year and the y-axes the hour of the day (UTC+2). The coloured pixels represent the f_{60} values. Note the different colour scales between the mean and median figures. It is also worth mentioning that due to the rather low signal to noise ratio of the ACSM, the f_{60} estimates can be very noisy. To avoid the weight of the high and low noise extremes in the a-panel (mean f_{60}), only the range of $0 \geq f_{60} \leq 1$ were included in the f_{60} mean field calculation.

- The following text has been added to chapter 3.1 *Inter- and intra-annual variation*:

69
70
71
72
73
74
75
76
77
78
79
80
81

Page 17, lines 517–530: “While the quantification and separation of BBOA from SOA will be the topic of an upcoming independent publication centred on the analysis of organic aerosol mass spectral fingerprints at SMEAR II, we briefly introduce the behaviour of f_{60} . f_{60} , which equals the contribution of m/Q 60 Th signal to the total organic signal recorded by the ACSM, is a marker for levoglucosan-like species originating from cellulose pyrolysis in biomass burning (Schneider et al., 2006;Alfarra et al., 2007). f_{60} is present at high percentages in fresh BBOA plumes (Cubison et al., 2011), but decays due to BBOA photochemical aging into oxidised organic aerosol. The fairly rapid (in order of several hours to days) photochemical aging of BBOA has been a topic of earlier chamber (Grieshop et al., 2009;Jimenez et al., 2009) and ambient studies (DeCarlo et al., 2010;Cubison et al., 2011). Here, unlike CO and eBC, f_{60} does not increase as a function of temperature in the highest temperature bins, but stays rather constant albeit lower than the f_{60} values recorded under cold temperatures at SMEAR II (Figure 5e). As the possible wild fires contributing to SMEAR II CO and eBC under high ambient temperatures also occur further away, it is likely that the BBOA is oxidised before detected at SMEAR II. CO and eBC can be considered as more inert BBOA markers compared to f_{60} . The wintertime f_{60} is likely linked to

82 wintertime biomass burning (for domestic heating purposes) emissions trapped in the shallow mixing layer.
83 These emissions are discussed more later on in the manuscript (see chapter 3.2 Diurnal variation of NR-PM₁
84 composition).”

85 - The following text has been added to chapter 3.1.1 *The effect of warm summers on organic aerosol loading:*

86 **Pages 18–19, lines 579–589:** “The f_{60} in turn follows the conclusions made earlier in the context of Figure 5, as
87 the f_{60} values remain low each July, and approach the f_{60} background levels of 0.3% (Cubison et al., 2011;
88 Figure 6e). Importantly, such negligible f_{60} signals were detected under the influence of an aged BBOA plume
89 originating from Moscow and Northern Ukraine wild fires at SMEAR II also in 2010 (Corrigan et al., 2013). An
90 AMS, which was used as one of the measurement tools in the campaign, detected mass spectra resembling
91 oxidised organic aerosol during the biomass burning influence. These data correlated well with multiple biomass
92 burning markers including CO, potassium and acetonitrile despite the lack of resemblance with fresh BBOA
93 mass spectra with high f_{60} . Corrigan et al. (2013) finally attributed up to 25% of the organic aerosol to BBOA
94 originating from the Moscow and Northern Ukraine wild fires. 35% of the organic aerosol mass was associated
95 with biogenic SOA formation. The weather during the Corrigan et al. (2013) study period in 2010 was also
96 unusually warm ($T_{avg} = 20^{\circ}\text{C}$), and resembled summers 2014 and 2018 also regarding the ruling anti-cyclonic
97 circulation.”

98
99 - We also want to inform the reviewer that we have added a figure of the Org/OC-ratio (~OM/OC) monthly
100 statistics from 2018 to the manuscript (Figure AR.6 which is Figure A.5 in the Appendix A: Supporting figures),
101 as well as colour coded Figure 2e by month of the year (Figure AR.5 which is Figure 2e in the manuscript) due
102 to the requests of Reviewer #3. The intra-annual variability of Org/OC also serves as additional chemical
103 information regarding OA composition (~degree of oxygenation). These changes are specified below in the line-
104 by-line response to Reviewer #3.

105 *Another issue is that this manuscript cites a lot of previous publications from SMEAR II but sometime without providing*
106 *sufficient contexts. Readers who are less familiar with the literature may feel somewhat lost or unconvinced.*

107 - We agree with the reviewer.

108

109 **Manuscript modifications:**

110

111 - We have added the following text under chapter 1 Introduction:

112

113 **Pages 4–5, lines 116–135:** “The chemical composition of aerosol particles at SMEAR II has been studied
114 previously in multiple short (<1 – 10 month) measurement campaigns with both offline (Saarikoski et al.,
115 2005;Kourtchev et al., 2005;Cavalli et al., 2006;Finessi et al., 2012;Corrigan et al., 2013;Kourtchev et al.,
116 2013;Kortelainen et al., 2017), and online methods (Allan et al., 2006;Finessi et al., 2012;Häkkinen et al.,
117 2012;Corrigan et al., 2013;Crippa et al., 2014;Hong et al., 2014;Makkonen et al., 2014;Äijälä et al., 2017;Hong
118 et al., 2017;Kortelainen et al., 2017;Riva et al., 2019;Äijälä et al., 2019). The previous studies include several
119 important discoveries regarding SMEAR II aerosol composition. For example, a large mass fraction of
120 particulate matter has been found to be (highly oxidised) organic aerosol (Corrigan et al., 2013;Crippa et al.,
121 2014;Äijälä et al., 2017;Äijälä et al., 2019), and recognised as terpene oxidation products (Kourtchev et al.,
122 2005;Allan et al., 2006;Cavalli et al., 2006;Finessi et al., 2012;Corrigan et al., 2013;Kourtchev et al., 2013). In
123 addition to this forest-generated SOA, a nearby sawmill can also significantly contribute to the OA loading in
124 the case of south easterly winds (e.g. Liao et al., 2011;Corrigan et al., 2013;Äijälä et al., 2017). The composition
125 of the sawmill-OA is found to significantly resemble biogenic SOA (Äijälä et al., 2017). Also, biomass burning
126 organic aerosol (BBOA) contributes to the OA mass (Corrigan et al., 2013; Crippa et al., 2014; Äijälä et al.,
127 2017; Äijälä et al., 2019). The BBOA presence in the summertime aerosol depends on long-range transport of
128 wildfire plumes. Inorganic species from anthropogenic activities, majority identified as ammonium sulphate and
129 nitrate, are also transported to the station. Ammonium sulphate represents the dominating inorganic species
130 (e.g. Saarikoski et al., 2005; Äijälä et al., 2019). Despite the long list of studies and discoveries, the
131 measurement/sampling periods have occurred mostly between early spring and late autumn, leaving the

132 description of the wintertime aerosol composition nearly fully lacking. Hence, based on these studies alone, the
133 understanding of the degree of variability in aerosol chemical composition at SMEAR II is incomplete – in both
134 intra- and inter-annual scales.”

136 *In addition, the creation of an Appendix section and the placement of several figures in there appear a bit haphazard and*
137 *may introduce confusion.*

138 - The purpose of the Appendix A is to provide supporting Figures to the main text.

139 **Manuscript modifications:**

140 - The Appendix A is now named appropriately: *Appendix A: Supporting figures.*

141 *More detailed comments are given below:*

142 *What type of interpretation was applied to the image plots in Figure 1?*

143 - The interpretation of Figure 1 is written in the section 2.1 under SMEAR II description. This section includes
144 the description of the meteorological conditions ruling at SMEAR II.
145 - Just in case the reviewer meant to ask about the *interpolation* method applied to the image plots, we will clarify
146 it, too: The figures were produced with the MATLAB 2017a “*contourf*” function. It performs the interpolation
147 in a linear manner to create isolines of matrix **M**, where **M** contains values (temperature, global radiation, wind
148 speed) on the *x-y* plane (month in year, hour in day). The selection of the isolines is performed automatically.
149 Due to the circular nature of wind direction, no interpolation was applied there. Figure 1c was produced with
150 MATLAB 2017a “*pcolor*” function. We now refer to the MATLAB 2017a *contourf*- and *pcolor*-functions in
151 the Figure 1 caption.

152 **Manuscript modifications:**

153 - **Figure 1 caption (page 6, lines 185–191):** *The seasonal evolution of diurnal cycles of ambient temperature*
154 *measured 4.2 m above ground level (panel a), global radiation above the forest canopy (panel b), wind direction*
155 *above the forest canopy (panel c), and wind speed above the forest canopy (panel d) recorded at SMEAR II*
156 *station in 2012 – 2018. The y-axes in the figures represent the local time of day (UTC+2) and the x-axes the*
157 *time of the year. The colour scales correspond to the temperature in degrees Celsius, global radiation in $W m^{-2}$,*
158 *wind direction in degrees and wind speed in $m s^{-1}$, respectively. Panels a, b and d include interpolation of the*
159 *$14 d \times 1 h$ resolution data grid into isolines based on the MATLAB2017a *contourf* function. Panel c has no*
160 *interpolation involved due to challenges related to interpolating over a circularly behaving variable. The plot is*
161 *produced with MATLAB 2017a *pcolor* function.*

162 *Line 182, change “evaporating at 600°C maximum” to “flash evaporate at 600°C”.*

163 **Manuscript modifications:**

164 - We changed the text as the reviewer suggested.

165 *Line 184, add “of” after “the signal”.*

166 **Manuscript modifications:**

167 - We changed the text as the reviewer suggested.

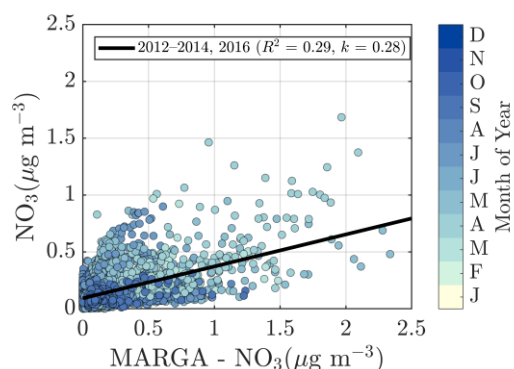
168 *Line 224, spell out the acronyms that have not yet been defined.*

169 **Manuscript modifications:**

170 - We changed the text as the reviewer suggested.

171 *Line 307, it is briefly mentioned that large discrepancies between ACSM nitrate and MARGA nitrate were observed, likely*
172 *introduced by organic nitrate. This is quite interesting, it would be helpful that the authors provide a bit more details and*
173 *expand the discussions.*

- 174 - The differences between MARGA and AMS nitrate measurements at SMEAR II have been already discussed in
 175 Makkonen et al. (2014). They address i) noise introduced by low mass concentration of nitrate, ii) organic
 176 nitrates, and iii) the possibility of un-optimal MARGA nitrate background subtraction as possible factors leading
 177 to measurement discrepancies. We chose not to compare the MARGA and ACSM nitrate concentration under
 178 the chapter 2.5 ACSM chemical speciation validation due to the known scatter between these measurements.
 179 Another possible factor weakening the nitrate correlation might also be a due to a time-to-time overestimation
 180 of the ACSM NO₃ caused by the presence of an organic fragment (i.e., CH₂O⁺) coinciding with NO⁺ at m/Q 30
 181 Th. Unfortunately, the unit mass resolution of the ACSM disables us from separating those ions, further forcing
 182 us to fully trust the default fragmentation table provided by Aerodyne Inc., the instrument manufacturer.
 183 However, as shown in Figure AR.3 low slope, this overestimation is likely not significant. Contrariwise, it is
 184 worth pointing out the differences in the ACSM and MARGA measurement size ranges (~PM₁ vs PM_{2.5}) that is
 185 the most likely reason for the low slope (k = 0.28) in the Figure AR.4 shown below.
 186 - The presence of organic nitrates is discussed later in the manuscript in terms of the nitrate fragmentation ratio
 187 (m/Q 30 Th : m/Q 46 Th), and visualised in Figure 7g.



188

189 **Figure AR.4** The ACSM nitrate vs the PM_{2.5} nitrate detected with MARGA–2S. The color coding represents the month of the year.
 190 The black line represents the overall linear fit. The figure can be found in the *Appendix A: Supporting figures: Figure A.3.*

191 **Manuscript modifications:**

- 192 - Figure AR.4, shown above, is added to *Appendix A: Supporting figures* (Figure A.3).
 193 - The following text is added to chapter 2.5 ACSM chemical speciation validation:

194

195 **Page 12, lines 398–409:** “Regarding the water-soluble inorganic ions, only the SO₄²⁻ concentration (in PM_{2.5}),
 196 retrieved from the MARGA measurements, was used for the current analysis for ACSM data validation purposes.
 197 The nitrate time series, for example, are known to be different between the two measurements at SMEAR II
 198 (Makkonen et al., 2014). The scatter between the nitrate measurements, visualised also here, in Figure A.3,
 199 could serve as evidence of organic nitrates, which are not efficiently detected by MARGA (Makkonen et al.,
 200 2014). The presence of organic nitrates is discussed later in the manuscript (see chapter 3.2 Diurnal variation
 201 of NR–PM₁ composition). Other factors influencing the nitrate agreement could arise from the MARGA nitrate
 202 background subtraction procedure, the overall low nitrate signal at SMEAR II (Makkonen et al., 2014), an
 203 organic CH₂O⁺ fragment coinciding with NO⁺ at m/Q 30 Th leading to ACSM nitrate over prediction under
 204 certain conditions, and finally the difference between the ACSM and MARGA size cuts (PM₁ vs PM_{2.5}). The
 205 ACSM sulphate, however, correlates well with MARGA (Pearson R² = 0.77), but has a slightly lower Pearson
 206 R² compared to an earlier < 11-month MARGA vs AMS comparison from SMEAR II (Pearson R² = 0.91)
 207 (Makkonen et al., 2014). Overall, based on the good agreement between ACSM and Sunset OCEC, MARGA,
 208 DMPS and Dekati cascade impactor measurements, we are confident of the year-to-year comparability of our
 209 ACSM dataset.”

210

- 211 - The following text is added to chapter 3.2 Diurnal variation of NR-PM₁ composition:

212 **Page 21, lines 676–678:** “Such high organic nitrate fraction could also explain some of the scatter observed in
 213 the ACSM NO₃ and MARGA NO₃ comparison discussed earlier in the manuscript (Figure A.3 and chapter 2.5
 214 ACSM chemical speciation validation).”

215 *Line 316 – 317. Is this sentence referring to the CE values used in this study or those typically used for ACSM*
216 *measurements?*

217 - The CE values refer to those typically used for AMS type of instrument.

218 **Manuscript modifications:**

219 - We clarified the statement.

220 *Line 322, give details on how DMPS-derived mass concentration is determined*

221 **Manuscript modifications:**

222 - The following details are now given in chapter 2.4 ACSM collection efficiency correction:

223 **Page 20, lines 351–356:** “The DMPS-derived mass concentration is determined as follows: i) calculation of
224 aerosol volume concentration ($m^3 m^{-3}$) of the ACSM detectable size range, where the aerodynamics lens
225 transmission is most efficient (50–450 nm in electrical mobility = ~75–650 nm in vacuum aerodynamic diameter)
226 and assuming spherical particles, ii) estimating aerosol density based on the ACSM-measured chemical
227 composition ($\rho_{(NH_4)_2SO_4} = 1.77 g cm^{-3}$, $\rho_{NH_4NO_3} = 1.72 g cm^{-3}$, $\rho_{org} = 1.50 g cm^{-3}$, $\rho_{BC} = 1.00 g cm^{-3}$), iii) calculating
228 the mass concentration ($\mu g m^{-3}$; mass concentration = density \times volume concentration).”

229

230 *Lines 328, 330, change “Figure 1a” to “Figure 2a”.*

231 **Manuscript modifications:**

232 - All the figure numberings were checked and corrected.

233 *Check the texts at Line 357 – 358.*

234 **Manuscript modifications:**

235 - The misplaced text was deleted.

236 *Figure 2 caption, check the text for (b)*

237 **Manuscript modifications:**

238 - The misplaced text was deleted.

239 *Figure 4, what’s the explanation for the large year-to-year variations in average SO₂ concentration?*

240 - The SO₂ concentration at SMEAR II is controlled by SO₂ sources (emissions), sinks
241 (photochemistry/heterogeneous oxidation to sulphate, wet and dry deposition), transport (general circulation
242 affecting wind direction and speed as well as SO₂ plume dispersion) and boundary layer meteorology
243 (temperature inversions trapping pollutants). The intra-annual variability of SO₂ concentration at SMEAR II is
244 likely a result from the variability of one or many of these factors. As can be seen from Figure 9e in the
245 manuscript, the elevated SO₂ concentrations (dark areas in the concentration field) are associated with very
246 specific, rather narrow ranges of ~easterly wind directions, and elevated wind speeds. This figure alone visualises
247 that the SMEAR II SO₂ concentration is *very sensitive* to even moderate wind direction (~analogous with air
248 mass trajectory) and speed variations. The Figure AR.5 demonstrates the wind direction variability in different
249 Februaries throughout the measurement period. The yellow shadings indicate the approx. wind direction areas
250 associated with elevated SO₂ loadings. The year-to-year variability in wind direction is significant, which can
251 certainly explain some of the intra-annual variability visualised in Figure 4 just in February. A more detailed
252 answer would require a comprehensive investigation on the variability of the different factors affecting SO₂
253 concentration that would require emission inventories, and modelling efforts.
254

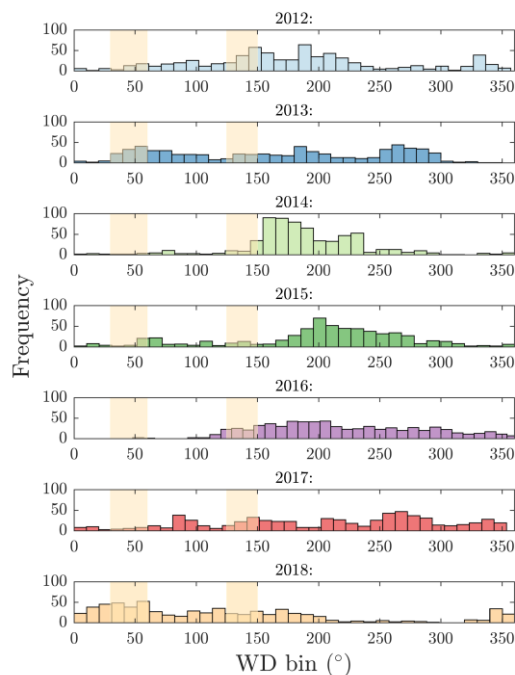


Figure AR.5 Wind direction histograms for each February of the measurement period (2012—2018). The yellow shaded areas indicate wind directions associated with high SO₂ anomalies at SMEAR II (Figure 9e). Note that this figure does not visualize the wind speed data that is often needed to exceed 20 km h⁻¹ for the SO₂ transport to occur efficiently (Figure 9e).

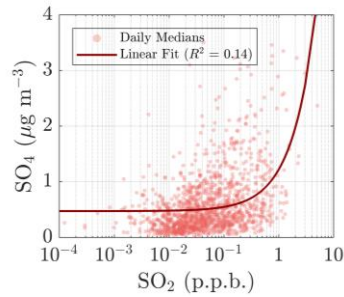
Manuscript modifications:

- We have added the following text to chapter 3.3.3 *Openair: Sulphate and SO₂*:

Page 27, lines 796–802: “As can be seen from Figures 9e, A.8e & A.9e, elevated SO₂ concentrations (dark areas in the concentration fields) are associated with very specific, rather narrow ranges of easterly (mainly NE and SE) wind directions, and elevated wind speeds (> 16 – 20 km h⁻¹). These figures illustrate the sensitivity of the recorded SO₂ concentration towards even moderate wind direction and speed variations. As wind direction and speed can vary significantly in an inter-annual scale, also inter-annual variability in SO₂ concentration can be expected. This could finally explain the SO₂ inter-annual variability highlighted especially in winter months (Figure 4e). Such strong variability is not reflected further in the sulphate aerosol (Figure 4b) year-to-year scales due to its long lifetime and build-up in the atmosphere.”

In 2017, SO₂ was nearly 0 in all months but sulfate concentration was not too much different than those in the other years. Why so?

- The link between SO₂ and sulfate is not easily shown with ambient data due to the long lifetime/ atmospheric build-up of sulfate aerosol, and the sensitivity of SO₂ concentration towards meteorological variability. This results in quite poor correlation between SO₂ and SO₄-aerosol at SMEAR II ($R^2 = 0.14$; Figure AR.6). The SO₂ concentration is generally elevated with easterly winds (Figure 9e in the manuscript), but also requires relatively high wind speeds (>20 km h⁻¹; Figure 9e) to diminish the SO₂ concentration decline during transport via photochemical or wet deposition sink pathways. The discrepancy mentioned by the reviewer between the detected SO₂ and SO₄ concentrations might be quantitatively explained with a comprehensive SO₂ emission inventory map together with detailed investigation of the meteorological conditions.



291 **Figure AR.6** The relationship between the SO₂ and particulate SO₄ concentrations at SMEAR II. Note the logarithmic scale on the
 292 x-axis.

293 **Manuscript modifications:**

- 294 - The topic has been reflected in the previous manuscript modification made:

295
 296 **Page 27, lines 799–802:** “As wind direction and speed can vary significantly in an inter-annual scale, also inter-
 297 annual variability in SO₂ concentration can be expected. This could finally explain the SO₂ inter-annual variability
 298 highlighted especially in winter months (Figure 4e). Such strong variability is not reflected further in the sulphate
 299 aerosol (Figure 4b) year-to-year scales due to its long lifetime and build-up in the atmosphere.”
 300

301 *Line 476, “exceptionally long-lasting period with high atmospheric pressure”, can this statement be a bit more*
 302 *quantitative, i.e., what does exceptionally long-lasting mean?*

- 303 - A more quantitative statement would require more detailed meteorological analysis on the pressure anomalies.

304 **Manuscript modifications:**

- 305 - We simplified the sentence and added a reference:

306
 307 **Page 17, lines 540–542:** “These summers were the hottest during the whole measurement period (Figure 6a),
 308 and linked to persistent high pressure conditions (Sinclair et al., 2019;FMI, 2014) “.

309 *Line 479, quote the 7 year mean July temperature.*

310 **Manuscript modifications:**

- 311 - Quoted.

312 *Line 699, what Figure c?*

313 **Manuscript modifications:**

- 314 - All the figure numberings were checked and corrected.

315 *Line 702, revise this sentence “ but shows . . . ”*

316 **Manuscript modifications:**

- 317 - Revised.

318

319

320 **Anonymous Referee #3**

321 *Received and published: 6 December 2019*

322 *The manuscript studies the sub-micron on-line aerosol composition at the research site of SMEAR II situated in the boreal*
323 *forest of Finland for a long period spanning from 2012 to 2018 using an Aerosol Chemical Speciation Monitor to derive*
324 *the inter- and intra-annual variability. Overall, organics represent the most abundant species, followed by sulphate,*
325 *nitrate and ammonium. PM₁ concentrations present a bimodal distribution peaking in February and in summer. The*
326 *winter peak is mostly linked to enhanced inorganic components such as nitrate and sulphate, while the summer maximum*
327 *is mostly linked to significant increase of organics, probably due to secondary organic aerosol formation. The study also*
328 *takes into account parameters such as temperature, insolation, wind speed and direction when interpreting the diurnal*
329 *and seasonal patterns of the different aerosol components. Finally two case studies are examined, derived from this inter-*
330 *and intra-annual variation, the enhanced concentrations during two summertimes (2014 and 2018) and enhanced*
331 *sulphate loadings during September 2014.*

332 *The paper is well written and easy to follow, though there are some issues and more thorough discussion should be made*
333 *in specific sections. Other than that the paper can be recommended for publication after addressing the issues listed*
334 *below.*

335 *General comments:*

336 *- There is overall an inconsistency in figure numbering and their reference within the text e.g. P11L330 Figure 1a should*
337 *be 2a and L338 should be figure 2b, P18L478 Figure4a should be 6a, P18L502 Figure d of which? Etc.*

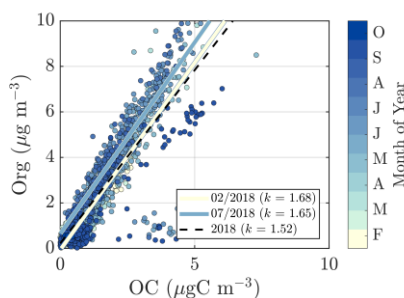
338 **Manuscript modifications:**

339 - All of the figure numberings checked and corrected.

340 *Specific comments:*

341 *- P12L361 It would be interesting to see whether OM/OC changes within the year as, e.g. SOA formation is expected to*
342 *lead to more oxidized species and thus, higher OM/OC. I would suggest maybe color-coding Figure 2e based on the date.*
343 *This would also be interesting further on in the manuscript, as 2018 is the case study having very warm summer (Section*
344 *3.1.1)*

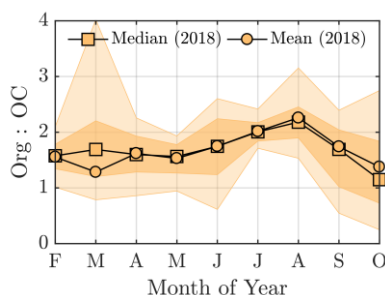
345 - The manuscript Figure 2e is now updated according to the reviewer's wishes (Figure AR.7). It now includes
346 color-coding based on the month of the year. Highest slopes (k) corresponding to the OM:OC are observed in
347 summer ($k = 1.65$ in July). The variability of slopes is rather small, as also wintertime OA is mainly highly aged
348 aerosol, notably also in winter (low-volatility oxygenated organic aerosol, LV-OOA; Heikkinen et al., 2020, *in*
349 *prep*).



350

351 **Figure AR.7** Updated manuscript Figure 2e. Organic carbon concentration (OC) vs the organic aerosol concentration (Org)
352 in 2018 at SMEAR II.

353 - As the OCEC Analyser was not functioning optimally most of the time, we are not including other years to the
354 analysis. Otherwise we could have compared the slopes (Org:OC values) in different summers to see if some
355 summers could have more influence from biomass burning, for example. However, if we plot the Org:OC
356 mean/median values, we observe a higher value in August 2018 compared to July 2018 which could indicate a
357 higher contribution of less oxidised OA in July (Figure AR.8).



358

359 **Figure AR.8** Organic carbon concentration (OC) vs the organic aerosol concentration (Org) in 2018 at SMEAR II. The darker yellow
 360 shadings indicate the area between the 25th and 75th percentiles and the lighter yellow the area between the 10th and 90th percentiles.
 361 The figure is added under *Appendix A: Supporting figures* as Figure A.5.

362 **Manuscript modifications:**

- 363 - Figure 2e updated with Figure AR.7 shown above.
 364 - Figure AR.8 added to *Appendix A: Supporting figures* as Figure A.5.
 365 - The following text is added to chapter 3.1.1 *Case study: The effect of warm summers on organic aerosol*
 366 *loading:*

367 **Page 18, lines 567–572:** “A quick revisit to the OC/EC vs ACSM comparison performed earlier in the
 368 manuscript (Figure 2e) shows relatively high Org/OC-values ($k = 1.68$) for July 2018, which further indicates
 369 of high oxygenation of OA (Aiken et al., 2008). However, the time series of the ruling monthly Org/OC-values
 370 visualised in Figure A.5 reveals an even higher Org/OC for August 2018. Further analysis of Org/OC recorded
 371 from SMEAR II is needed to answer whether such behaviour is frequently occurring at SMEAR II, or whether
 372 July 2018 organic aerosol was less functionalised (oxidised) than usual due to higher presence of primary
 373 organic aerosol, such as BBOA, than usual.”

- 374 - The following text is added to chapter 3.2 *Diurnal variation in NR-PM₁ composition:*

375 **Page 20, lines 654–656:** “Such conclusions can also be made based on the rather high Org/OC linear regression
 376 slope for February data ($k = 1.65$) depicted in Figure 2e (see also Figure A.5). As mentioned earlier, a high
 377 Org/OC-ratio indicates a higher degree of functionalisation/oxidation of organic aerosol (Aiken et al., 2008).”

378 *Technical corrections:*

- 379 - P12L357-358 *There seems to be something wrong with this sentence and what is inside the parenthesis.*

380 **Manuscript modifications:**

- 381 - Misplaced text removed.
 382 - P18L504 *only one week (delete “ca”)*

383 **Manuscript modifications:**

- 384 - ‘ca’ removed from the sentence.

385

386 **Other manuscript modifications**

387 - The following text was added to chapter 3.3.3 *Openair: Sulphate and SO₂* to include few Finnish national SO₂
388 sources to the discussion:

389 **Page 26, lines 765–770:** *“In addition to the major emission sources introduced by Riuttanen et al. (2013), also*
390 *paper and pulp industry are major known SO₂ emitters. Several paper and pulp mills are situated in Finland,*
391 *mostly NE and SE from SMEAR II (Metsäteollisuus, 2018). Another national major SO₂ source is certainly the*
392 *Kilpilahti (Porvoo) oil refinery, located ~200 km S-SE from SMEAR II. This area represents the most extensive*
393 *oil refinery and chemical industry in the Nordic countries, and the SO₂ concentrations measured downwind from*
394 *the area have been close to those obtained from Kola Peninsula outflow (Sarnela et al., 2015).”*

395

Long-term sub-micron aerosol chemical composition in the boreal forest: inter- and intra-annual variability

Liine Heikkinen¹, Mikko Äijälä¹, Matthieu Riva^{1,2}, Krista Luoma¹, Kaspar Dällenbach¹, Juho Aalto³, Pasi Aalto¹, Diego Aliaga¹, Minna Aurela⁴, Helmi Keskinen¹, Ulla Makkonen⁴, Pekka Rantala¹, Markku Kulmala¹, Tuukka Petäjä¹, Douglas Worsnop^{1,5}, and Mikael Ehn¹

¹Institute for Atmospheric and Earth System Research /Physics, Faculty of Science, University of Helsinki, Helsinki, FI-00014, Finland

²Univ Lyon, Université Claude Bernard Lyon 1, CNRS, IRCELYON, 69626, Villeurbanne, France

³Institute for Atmospheric and Earth System Research /Forest Sciences, Faculty of Agriculture and Forestry, University of Helsinki, Helsinki, FI-00014, Finland

⁴Atmospheric Composition Research, Finnish Meteorological Institute, Helsinki, FI-00101, Finland

⁵Aerodyne Research Inc., Billerica, MA, USA

Correspondence to: Liine Heikkinen (liine.heikkinen@helsinki.fi) and Mikael Ehn (mikael.ehn@helsinki.fi)

Abstract.

The Station for Measuring Ecosystem Atmosphere Relations (SMEAR) II is well known among atmospheric scientists due to the immense amount of observational data it provides of the earth–atmosphere interface. Moreover, SMEAR II plays an important role in large European research infrastructures, enabling the large scientific community to tackle climate and air pollution related questions, utilising the high-quality long-term data sets recorded at the site. So far, the well-documented site was missing the description of the seasonal variation of aerosol chemical composition that is crucial for understanding the complex biogeochemical and -physical processes governing the forest ecosystem. Here, we report the sub-micron aerosol chemical composition and its variability utilising data measured between 2012 and 2018 using an Aerosol Chemical Speciation Monitor (ACSM). We observed a bimodal seasonal trend in the sub–micron aerosol concentration culminating in February (2.7, 1.6, 5.1 $\mu\text{g m}^{-3}$ for median, 25th, 75th percentiles, respectively) and July (4.2, 2.2, and 5.7 $\mu\text{g m}^{-3}$ for median, 25th, 75th percentiles, respectively). The wintertime maximum was linked to an enhanced presence of inorganic aerosol species (ca. 50%) whereas the summertime maximum (ca. 80% organics) to biogenic secondary organic aerosol (SOA) formation. During the exceptionally hot Julys of 2014 and 2018, the organic aerosol concentrations were up to 70% higher than the 7–year July mean. The projected increase of heat wave frequency over Finland will most likely influence the loading and chemical composition of aerosol particles in the future. Our findings suggest strong influence of meteorological conditions such as radiation, ambient temperature, wind speed and direction on aerosol chemical composition. To our understanding, this is the longest time series reported describing the aerosol chemical composition measured online in the boreal region, but the continuous monitoring will be maintained also in the future.

1 Introduction

Both climate change and air pollution represent global grand challenges. Detailed monitoring of environments showing vulnerability towards them is crucial. The arctic and boreal forest are examples of such regions (Prävälje, 2018; Kulmala, 2018). The boreal forest represents ~15% of the Earth’s terrestrial area, spanning between 45 and 70 °N, and making up ~ 30% of the world’s forests (Prävälje, 2018). Over the course of the predicted warming, the boreal forest is likely to

39 move further north, resulting in arctic greening. In addition, the presence of southerly tree species are projected to increase
40 in the southern regions of the biome (Settele et al., 2014). These large-scale changes are linked to numerous complex
41 biogeochemical and -physical processes. These complexities greatly hamper our ability to make detailed predictions of
42 future changes, as exemplified by diversities in global model outputs of many important ecosystem- and climate-relevant
43 parameters (Fanourgakis et al., 2019). To help improve and constrain modelling efforts, comprehensive long-term high-
44 quality observational data are of utmost importance (Kulmala, 2018). Among the important parameters to monitor,
45 atmospheric composition, including both gaseous and particulate matter, provides a crucial link between the ecosystems
46 and climate.

47
48 Atmospheric aerosol particles affect Earth's radiative balance, influence ecosystems and human health, and reduce
49 visibility (Ramanathan et al., 2001;Boucher et al., 2013;Myhre et al., 2013). These particles can be emitted directly into
50 the atmosphere or form through gas-to-particle transition reactions from atmospheric vapours (Kulmala et al., 2004). The
51 composition of atmospheric aerosol particles has an extensive degree of variability depending on their origin. Their
52 composition covers a wide range of organic and inorganic species with differing physicochemical properties. These
53 properties affect the aerosol-related disturbances on the Earth's radiative forcing as salt particles scatter radiation
54 efficiently, whereas soot particles absorb it. In addition to this direct radiative effect, aerosol particles also participate in
55 cloud formation and processing. Indeed, every cloud droplet forms from an aerosol particle seed, termed a cloud
56 condensation nucleus (CCN). Moreover, these cloud seeds are often hygroscopic, which is directly linked to their
57 chemical composition. Important contributors to discrepancies estimating aerosol sensitivity of the boreal climate are
58 challenges in reproducing observations of aerosol chemical composition and properties (Fanourgakis et al., 2019).

59
60 Solar radiation and ambient temperature control both biogenic and human (anthropogenic) behaviour. In the northern
61 latitudes, the amount of radiation varies considerably in the course of a year yielding a large seasonal variation in ambient
62 temperature. The ambient temperature also fluctuates notably in diurnal scale. Ambient temperature influences emissions
63 of various biogenic volatile organic compounds (BVOCs) including monoterpenes (Guenther et al., 1993), whereas solar
64 radiation enables the photochemical reactions leading to oxidation products having lower volatilities. Secondary organic
65 aerosol (SOA) is formed from the partitioning of oxidised VOCs to the condensed phase. SOA is a key component in
66 tropospheric PM worldwide (Zhang et al., 2007a;Jimenez et al., 2009). While warmer conditions promote the emissions
67 of BVOCs, cold temperatures enhance the need of residential heating leading to emissions of primary particles as well as
68 a large variety of anthropogenic trace gases.

69
70 The major inorganic sub-micron aerosol species, of which the majority also originate from anthropogenic activities, are
71 sulphate, nitrate and ammonium (Zhang et al., 2007b;Jimenez et al., 2009). The presence of sulphur dioxide (SO₂), emitted
72 to the atmosphere from industrial processes and volcanic activity, has significantly increased compared to pre-industrial
73 conditions (Tsigaridis et al., 2006). It forms sulphuric acid upon oxidation that besides participating in the formation of
74 new particles, also readily condenses onto pre-existing aerosol particles increasing the particle mass loading and
75 ultimately modifying the acidity of atmospheric particles. Ammonia (NH₃), emitted in large quantities from industry and
76 agriculture, can partly neutralise particulate sulphuric acid forming ammonium sulphate, acknowledged as one of the
77 main contributors to sub-micron aerosol mass. In addition, ammonium nitrate, formed from the reaction between
78 ammonia and nitric acid is a common inorganic PM constituent. Nitrogen oxides (NO_x = NO + NO₂) from traffic

79 emissions and industry are the major nitric acid precursors in the atmosphere. These radicals play an important role in
80 atmospheric chemistry due to their high reactivity.

81

82 The concentrations of primary aerosol particles and the aerosol precursors (such as NO_x, NH₃, SO₂, and (B)VOCs) vary
83 during the year especially in the northern latitudes, where temperature differences between summer and winter are drastic.
84 Besides differences in the emissions, also the dynamics (thickness) of the atmospheric boundary layer influences airborne
85 pollutant concentrations. For example, during sunny summer days the boundary layer height can exceed two kilometres
86 height in the Northern hemisphere (McGrath-Spangler and Denning, 2013), and emissions from the surface are widely
87 dispersed in a large volume. During wintertime, the boundary layer can be more than a kilometre shallower than in
88 summer, and the pollutant loadings become concentrated closer to the surface. The boundary layer thickness is determined
89 by atmospheric stability. In unstable conditions, the air is rising and well mixed due to heating from below. In stable
90 conditions, generally caused by cooling from below, turbulence is suppressed and mixing occurs only close to the Earth's
91 surface. Shallow, nocturnal boundary layers are often stable due to radiative cooling from the Earth's surface.

92

93 To conclude, the aerosol chemical composition and loading in the lower troposphere are highly dependent on different
94 emission sources and meteorological conditions. As these vary over the course of a year, also seasonal variation can be
95 expected in aerosol composition and loading. Importantly, variation also occurs invariably in inter-annual scale. For
96 example, year-to-year variation in ambient temperature is normal, but expected to increase with increased frequency of
97 climate extremes introduced by climate change (Pachauri and Meyer, 2014; Kim et al., 2018). Such variations could affect
98 air pollutant loadings in the boreal region, as milder winters might lead to a decrease of emissions from domestic wood
99 burning, and warmer summers might enhance the emissions from frequent and intense wild fires as well as promote SOA
100 formation from oxidised BVOCs. Inter-annual variability in aerosol composition and loading can also be introduced by
101 emission regulations. For example, atmospheric PM₁₀, PM_{2.5}, SO₂ and NO_x concentrations have shown decreasing trends
102 in the past decades in United States and Europe (Wang et al., 2012; Aas et al., 2019; Anttila and Tuovinen, 2010; Simon et
103 al., 2014). Hence, for a well representative overview of aerosol climatology, and to truly capture seasonal variations
104 regarding air pollutants in the ruling boreal climate, a long-enough time series is required for analysis. Only then, a good
105 overview can be given of trends, variability, and seasonal and diurnal cycles of aerosol concentrations and composition.

106

107 The current study focuses on the seasonal variation of aerosol chemical composition and its year-to-year fluctuation at
108 the Station for Measuring Ecosystem – Atmosphere relations (SMEAR) II (Hari and Kulmala, 2005), located in the boreal
109 forest of Finland. The measurement period spans over seven years. SMEAR II is well known for its comprehensive,
110 simultaneous measurements tracking >1000 different environmental parameters within the Earth-atmosphere interface
111 covering forest, wetland and lake areas (Hari and Kulmala, 2005). Furthermore, SMEAR II is part of large research
112 networks such as Aerosols, Clouds and TRace gases InfraStructure (ACTRIS), Integrated Carbon Observation System
113 (ICOS), Europe's Long-term Ecosystem Research (LTER) and the infrastructure for Analysis and Experimentation on
114 Ecosystems (AnaEE).

115

116 The chemical composition of aerosol particles at SMEAR II has been studied previously in multiple short (<1 – 10 month)
117 measurement campaigns with both offline (Saarikoski et al., 2005; Kourtchev et al., 2005; Cavalli et al., 2006; Finessi et
118 al., 2012; Corrigan et al., 2013; Kourtchev et al., 2013; Kortelainen et al., 2017), and online methods (Allan et al.,

119 2006;Finessi et al., 2012;Häkkinen et al., 2012;Corrigan et al., 2013;Crippa et al., 2014;Hong et al., 2014;Makkonen et
120 al., 2014;Äijälä et al., 2017;Hong et al., 2017;Kortelainen et al., 2017;Riva et al., 2019;Äijälä et al., 2019). The previous
121 studies include several important discoveries regarding SMEAR II aerosol composition. For example, a large mass
122 fraction of particulate matter has been found to be (oxidised) organic aerosol (Corrigan et al., 2013;Crippa et al.,
123 2014;Äijälä et al., 2017;Äijälä et al., 2019), and recognised as terpene oxidation products (Kourtchev et al., 2005;Allan
124 et al., 2006;Cavalli et al., 2006;Finessi et al., 2012;Corrigan et al., 2013;Kourtchev et al., 2013). In addition to this forest-
125 generated SOA, a nearby sawmill also contributes significantly to the OA loading in the case of south easterly winds (e.g.
126 Liao et al., 2011;Corrigan et al., 2013;Äijälä et al., 2017). The composition of the sawmill-OA is found to significantly
127 resemble biogenic OA (Äijälä et al., 2017). Also biomass burning organic aerosol (BBOA) contributes to the OA mass
128 (Corrigan et al., 2013; Crippa et al., 2014; Äijälä et al., 2017; Äijälä et al., 2019). The BBOA presence in the summertime
129 aerosol depends on long-range transport of wildfire plumes. Inorganic species from anthropogenic activities, majority
130 identified as ammonium sulphate and nitrate, are also transported to the station. Ammonium sulphate represents the
131 dominating inorganic species (e.g. Saarikoski et al., 2005; Äijälä et al., 2019). Despite the long list of studies and
132 discoveries, the measurement/sampling periods have occurred mostly between early spring and late autumn, leaving the
133 description of the wintertime aerosol composition nearly fully lacking. Hence, based on these studies alone, the
134 understanding of the degree of variability in aerosol chemical composition at SMEAR II is incomplete – in both intra-
135 and inter-annual scales.

136

137 Here, we provide a comprehensive overview of sub-micron aerosol chemical composition at SMEAR II. This study does
138 not only provide the analysis of the longest time series of sub-micron aerosol chemical composition measured on-line in
139 the climate-sensitive boreal environment, but also introduces the data set to the scientific community for further utilisation
140 with other SMEAR II, ACTRIS, ICOS, LTER and AnaEE data to improve our understanding of the aerosol sensitivity of
141 the (boreal) climate.

142 **2 Measurements and methods**

143 In this chapter, we introduce the SMEAR II measurement site, data processing and analysis tools. As the meteorological
144 conditions ruling at the station are of high importance influencing sub-micron aerosol chemical composition, we will first
145 focus on giving an overview of the SMEAR II climate. The instrument operation, data processing and analysis part briefly
146 describes the instrumentation used, focusing mainly on the aerosol chemical speciation monitor (ACSM) that serves as
147 the key instrument for the current study.

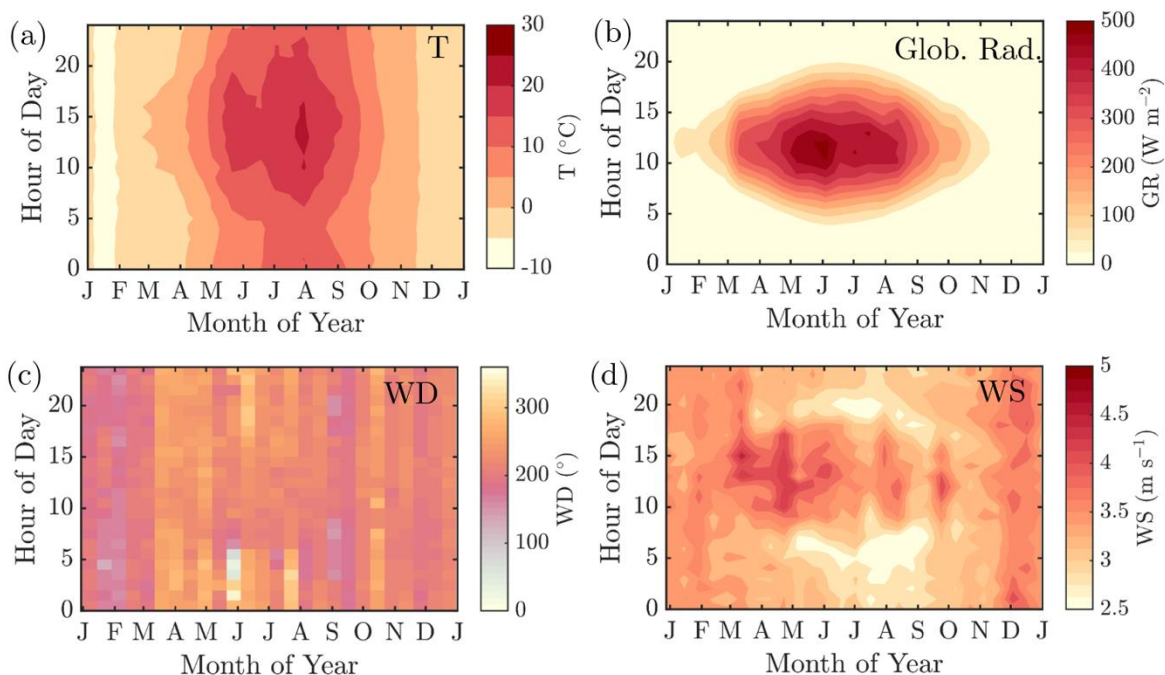
148 **2.1 SMEAR II description**

149 The measurements reported here were conducted at the SMEAR II station (61°51'N, 24°17'E, 181 m above sea level)
150 (Hari and Kulmala, 2005) between years 2012 and 2018. However, they continue also after 2018 as part of the station's
151 long-term measurements. SMEAR II is located in a nearly 60-year-old Scots pine (*Pinus sylvestris*) dominated stand. A
152 previous land use survey reveals that a majority of the area surrounding the station is forested, as 80% of the land within
153 5 km radius and 65% within 50 km radius is covered by mixed forest (Williams et al., 2011). The forested area located
154 north west of the station is shown to have least anthropogenic air pollutant sources (Williams et al., 2011;Tunved et al.,
155 2006). However, 90% of the forests in Fennoscandia region are introduced to anthropogenic influence via forest
156 management (Gauthier et al., 2015). The city of Tampere (population approximately 235 000) lies within the 50 km radius

157 to the south west introducing a notable source of anthropogenic pollution. Other evident nearby sources of anthropogenic
158 pollution are the town of Orivesi (population approximately 9 200) 19 km south of SMEAR II and the nearby village of
159 Korkeakoski with two saw mills and a pellet factory 6–7 km to the south east from SMEAR II (Liao et al., 2011;Äijälä et
160 al., 2017). Nonetheless, the dominating source of air pollutants are air masses advected from industrialized areas over
161 southern Finland, St. Petersburg region in Russia and continental Europe (Kulmala et al., 2000;Patokoski et al.,
162 2015;Riuttanen et al., 2013). The anthropogenic emissions are minor at the station. Monoterpenes, notably α -pinene and
163 Δ^3 -carene, are the dominating emitted biogenic non-methane VOCs from the forest (Hakola et al., 2012;Barreira et al.,
164 2017).

165

166 The mean annual temperature at the measurement station during the measurement period (2012–2018), recorded at 4.2 m
167 above ground level, was 5.4 °C. In average, January was the coldest month ($T_{\text{avg}} = -6.2$ °C) and July the warmest ($T_{\text{avg}} =$
168 16.6 °C). The mean annual temperature recorded was ca. 2°C higher than the 1981–2010 annual mean reported (Pirinen
169 et al., 2012). The seasonal and diurnal variation of temperature is presented in [Figure 1a](#) followed by the corresponding
170 data for global radiation above the forest ([Figure 1b](#)). November and December were the darkest months whereas the
171 radiation maximum was reached in late May and early June, which is earlier than generally observed at the top of the
172 atmosphere. The reason for the early radiation maximum peaking time is the increased fractional cloud cover in July
173 (Tuononen et al., 2019), likely promoted by convection. The formation of convective clouds hinders the transmission of
174 solar radiation to the lower troposphere, and increases the intensity of precipitation, making the 1981–2010 mean
175 precipitation maximum occur in July (92 mm) (Pirinen et al., 2012). However, November, December and January hold
176 the greatest amount of precipitation days (≥ 0.1 mm for ca. 21 days per month). The annual 1981–2010 mean cumulative
177 precipitation is 711 mm (Pirinen et al., 2012). The first snow on the ground can be expected in November, and the snow
178 depth maximum is commonly reached in March. The snow cover is roughly lost in April (Pirinen et al., 2012). The wind
179 direction recorded above the forest canopy during the measurement period is normally from the south west with enhanced
180 southerly influence during winter months (especially in January and February) and has large scatter during summer
181 months ([Figure 1c](#)&[Figure A.1a-c](#)). The diurnal mean of wind speeds above the forest canopy were usually greatest during
182 wintertime as can be expected based on overall Northern hemispheric behaviour. The seasonal cycles of wind speed show
183 most diurnal variability from May to September ([Figure 1d](#)&[Figure A.1a-c](#)).



184

185 **Figure 1** The seasonal evolution of diurnal cycles of ambient temperature measured 4.2 m above ground level (panel a), global
 186 radiation above the forest canopy (panel b), wind direction above the forest canopy (panel c), and wind speed above the forest canopy
 187 (panel d) recorded at SMEAR II station in 2012 – 2018. The y-axes in the figures represent the local time of day (UTC+2) and the x-
 188 axes the time of the year. The colour scales correspond to the temperature in degrees Celsius, global radiation in W m^{-2} , wind direction
 189 in degrees and wind speed in m s^{-1} , respectively. Panels a, b and d include interpolation of the $14 \text{ d} \times 1 \text{ h}$ resolution data grid into
 190 isolines based on the MATLAB2017a *contourf* function. Panel c has no interpolation involved due to challenges related to interpolating
 191 over a circularly behaving variable. The plot is produced with MATLAB 2017a *pcolor* function.

192

193 2.2 ACSM measurements

194 The Aerosol Chemical Speciation Monitor (ACSM; Aerodyne Research Inc. USA) was first described by Ng et al. in
 195 2011. It was developed based on the Aerosol Mass Spectrometer (AMS) (Canagaratna et al., 2007), but simplified at the
 196 cost of mass and time resolution to achieve a robust instrument for long-term measurements. The ACSM samples ambient
 197 air with a flow rate of $1.4 \text{ cm}^3 \text{ s}^{-1}$ through a critical orifice (100 μm in diameter) towards an aerodynamic lens efficiently
 198 transmitting particles between approximately 75 and 650 nm in vacuum aerodynamic diameter (D_{va}) and pass through
 199 particles further up to $1 \mu\text{m}$ in D_{va} with a less efficient transmission (Liu et al., 2007). After this, the particles are flash
 200 vaporized at a 600 °C hot surface in high vacuum and ionised with electrons from a tungsten filament (70 eV, electron
 201 impact ionisation, EI). These processes lead to substantial fragmentation of the molecules forming the aerosol particles.
 202 The resulting ions are guided to a mass analyser, a residual gas analyser (RGA) quadrupole, scanning through different
 203 mass-to-charge ratios (m/Q). The detector is a secondary electron multiplier (SEM). The particulate matter detected by
 204 the ACSM is referred to as non-refractory (NR) sub-micron particulate matter (PM_1). The word 'non-refractory' (NR)
 205 is attributed to the instrument limitation to detect material flash evaporating at 600 °C thus being unable to measure heat-
 206 resistant material such as minerals or soot. The word ' PM_1 ' is linked to the aerodynamic lens approximate cut-off at 1
 207 μm . Importantly, the NR- PM_1 reported from these ACSM measurements is a difference between the signal of particle-
 208 laden air and signal recorded when the sampling flow passed a particle filter (filtered air).

209

210 The ACSM measurements for the current study were conducted within the forest canopy through the roof of an air
211 conditioned container. A PM_{2.5} cyclone was used to filter out big particles that could cause clogging of the critical orifice.
212 A Nafion dryer was installed in 2013 upstream the instrument ensuring a sampling relative humidity (RH) below 30%.
213 Before this, the RH was not controlled nor recorded. Thus, the RH was likely high during summer, but low during
214 wintertime. Moreover, a 3 litres per minute (Lpm) overflow, which was ejected only before the aerodynamic lens, was
215 used to minimise losses in the sampling line (length approximately 3 m). The data were acquired using the ACSM data
216 acquisition software (DAQ) provided by Aerodyne Research Inc., the instrument manufacturer. The DAQ version was
217 updated upon new releases. The ACSM was operated to perform m/Q scans with a 200 ms Th⁻¹ scan rate in the mass-to-
218 charge range of m/Q 10 Th to 140 Th. Filtered and particle-laden air were measured interchangeably for 28 quadrupole
219 scans resulting in ca. 30 minute averages. The air signal, obtained from the automatic filter measurements, was subtracted
220 from the sample raw signal, yielding the signal from aerosol mass only. The data processing was performed using ACSM
221 Local v. 1.6.0.3 toolkit within the Igor Pro v. 6.37 (Wavemetrics Inc., USA). Upon data processing, the different detected
222 ions were assigned into organic or inorganic species bins (i.e. total organics, sulphate, nitrate, ammonium and chloride)
223 using a fragmentation table (Allan et al., 2004). Moreover, the data were normalized to account for N₂ signal variations
224 related to ACSM flow rate and sensitivity changes (due to SEM voltage response decay).

225

226 The ACSM raw signal (IC) is converted to mass concentration (C) with the following equation obtained from Ng et al.
227 (2011):

228

$$C_s = \frac{1}{CE \times T_{m/Q}} \times \frac{10^{12}}{RIE_s \times RF_{NO_3}} \times \frac{Q_{cal} \times G_{cal}}{Q \times G} \times \sum_{i=0}^n IC_{s,i} \quad (1)$$

229

230 where C_s is the concentration of species s , CE is the particle collection efficiency (see chapter 2.4 ACSM collection
231 efficiency correction), and $T_{m/Q}$ the m/Q -dependent ion transmission efficiency in the RGA quadrupole mass analyser.
232 The $T_{m/Q}$ is constantly recorded based on naphthalene fragmentation patterns and their comparison to naphthalene
233 fragmentation pattern in the NIST data base (75 eV EI; <http://webbook.nist.gov/>). Naphthalene is used as an internal
234 standard in the ACSM and is thus always present in the mass spectrum (Ng et al., 2011). The RIE_s is the relative ionisation
235 efficiency of species s and RF_{NO_3} the ACSM response factor determined through ionisation efficiency (IE) calibrations
236 with ammonium nitrate (NH₄NO₃). The RF_{NO_3} explains the ACSM ion signal (A) per $\mu\text{g m}^{-3}$ of nitrate. Q_{cal} and G_{cal} are
237 the ACSM volumetric flow rate and detector gain during ACSM calibration, whereas Q and G are the values during the
238 measurement period for volumetric flow rate and detector gain, respectively. They generally correspond the calibration
239 values. The final parameter is the sum of the signal introduced by individual ions ($IC_{s,i}$) originating from species s .

240

241 The ionisation efficiency calibration was performed with dried and size-selected ammonium nitrate (NH₄NO₃) particles
242 to retrieve the RF_{NO_3} parameter required in Equation (1). In addition, ammonium sulphate ((NH₄)₂SO₄) calibrations were
243 carried out, albeit less frequently, providing a value for the sulphate relative ionization efficiency (RIE_{SO_4}). RIE_{NH_4} was
244 derived from the ammonium nitrate calibration. Constant RF and RIE values were used for each year, respectively. The
245 conversion from ACSM raw signal to mass concentration was performed with the ACSM Local v. 1.6.0.3 provided by
Aerodyne Research Inc.

246 **2.3. Additional measurements**

247 In addition to the ACSM-measurements, the SMEAR II station has a large number of other air composition related
248 measurements. In the current study, we investigate only a small fraction of them. The particle measurements (i.e. ACSM,
249 Differential Mobility Particle Sizer (DMPS), Dekati cascade impactor, Aethalometer, Organic Carbon and Elemental
250 Carbon (OCEC) analyser and Monitor for AeRosols and Gases in ambient Air (MARGA) 2S) were conducted in two
251 measurement containers and a cabin, all located within ca. 50 m from each other. The gas phase sampling of NO_x, SO₂,
252 CO and VOCs as well as temperature, wind and global radiation measurements, were conducted from the station mast
253 that has several measurement heights from near ground to 127 m height. The temperature measurement was conducted
254 with a Pt100 sensor (4.2 m above ground level), the global shortwave radiation with a Middleton SK08 pyranometer (125
255 m above ground level). The horizontal wind measurements were conducted with Thies 2D Ultrasonic anemometers above
256 the forest canopy (16.8 to 67.2 m above ground level). The NO_x measurements were performed with a TEI 42 iTL
257 chemiluminescence analyser equipped with a photolytic Blue Light Converter (NO₂* to NO*) converter, SO₂ with a TEI
258 43 iTLE fluorescence analyser, and CO with IR absorption analysers Horiba APMA 370 (until January 2016) and API
259 300EU (from February 2016 onwards). The NO_x, SO₂, CO and PTR-MS sampling was conducted 67.2 m above ground
260 level. The SO₂, NO_x, CO, and PTR-MS (only 2012–2013), and meteorology data were uploaded from Smart-SMEAR
261 data base (<https://avaa.tdata.fi/web/smart>) (Junninen et al., 2009). The DMPS, Dekati impactor, Aethalometer, OCEC-
262 analyser and MARGA-2S measurements were conducted within the forest canopy are described in more detail in the
263 sections below. The data availability is shown in [Figure A.2](#).

264 **2.3.1 DMPS**

265 The Differential Mobility Particle Sizer (DMPS) measures the aerosol size distribution below 1 µm electrical mobility
266 diameter. SMEAR II holds the world record in online aerosol size distribution measurements (Dada et al., 2017), as the
267 measurements started already in 1996. The DMPS system is described in detail previously (Aalto et al., 2001). Briefly,
268 the SMEAR II DMPS is a twin DMPS setup that samples 8 m above ground from an inlet with a flow rate of 150 Lpm.
269 The measurement cycle is 10 minutes. The first DMPS (DMPS-1) has a 10.9 cm long Vienna type differential mobility
270 analyser (DMA) and a model TSI3025 condensation particle counter (CPC) that was changed to model TSI3776 after
271 October 2016. The sheath flow rate in the DMA is 20 Lpm and aerosol flow rate 4.0 Lpm. The measurement range of the
272 DMPS-1 is 3–40 nm. The second DMPS (DMPS-2) has a 28 cm long Vienna type DMA and a TSI3772 CPC. The sheath
273 flow rate is 5 Lpm and the aerosol flow rate 1 Lpm. The measurement range is 20 nm – 1 µm. The sheath flows are dried
274 (RH < 40%), and controlled with regulating valves as well as measured with TSI mass flow meters operated in volumetric
275 flow mode. The aerosol flow is brought to charge balance with 370 MBq C-14, and after March 2018 with a 370 MBq
276 Ni-63 radioactive beta source. The aerosol flow rates are monitored with pressure drop flow meters. The aerosol flows
277 were not dried. Temperatures and RHs are monitored from DMPS excess flow and from the aerosol inlet. The aerosol
278 flow rates were checked and adjusted every week against a Gilian Gilibrator flow meter throughout the measurement
279 period. The DMA high voltages were also validated with a multimeter. The CPC concentrations were compared against
280 each other with size-selected ammonium sulphate particles in the 6–40 nm range as well as compared against the TSI3775
281 particle counter that measures the total aerosol particle number concentration at the station. The sizing accuracy of the
282 two DMAs were cross-compared with 20 nm ammonium sulphate particles. In addition, the accuracies of the RH,
283 temperature and pressure probes were validated each year.

284 2.3.2 Cascade impactor

285 The PM₁ and PM_{2.5} (particulate mass of aerosol particles with an aerodynamic diameter below 2.5 μm) mass
286 concentrations measured between 2012–2017, which were included in the current study, were retrieved from the cascade
287 impactor measurements. This gravimetric PM₁₀ impactor, produced by Dekati Ltd., is a three-stage impactor with cut-
288 points at 10, 2.5 and 1 μm. The collection is conducted on greased (Apiezon vacuum grease diluted in toluene) Nuclepore
289 800 203 25 mm polycarbonate membranes with 30 Lpm flow rate, approximately 5 m above ground level. The filter
290 smearing was performed to avoid losses due to particle bouncing. The filters were weighed manually every 2–3 days and
291 stored in a freezer for possible further analysis.

292 2.3.3 PTR–MS

293 The monoterpene concentration was measured using the proton transfer reaction quadrupole mass spectrometer (PTR–
294 MS) manufactured by Ionicon Analytik GmbH, Innsbruck, Austria (Lindinger and Jordan, 1998). The monoterpene
295 measurement setup is described in detail previously (Rantala et al., 2015). Shortly, the PTR–MS was placed inside a
296 measurement cabin on the ground level and the sample air was drawn down from a measurement mast to the instrument
297 using a 157 m long PTFE tubing (16/14 mm o.d./i.d.). The sampling line was heated and the sample flow was 45 Lpm.
298 However, the sample entering the PTR–MS was only 0.1 Lpm. During the study period, the primary ion signal H₃O⁺
299 (measured at isotope *m/Q* 21 Th) varied slightly around 5–30 × 10⁶ c.p.s. (counts per seconds). The instrument was
300 calibrated every 2–4 weeks using three different VOC standards (Aper–Riemer) and the instrumental background was
301 measured every third hour using VOC free air, produced by a zero air generator (Parker ChromGas, model 3501).
302 Normalised sensitivities and the volume mixing ratios were then calculated using the method introduced previously
303 (Taipale et al., 2008). For example, the normalized sensitivity of alpha-pinene (measured at *m/Q* 137 Th) varied between
304 2 and 5 n.c.p.s. p.p.b.⁻¹ over the study period. Only the signal of monoterpenes at *m/Q* 137 Th were analysed in the current
305 study.

306 2.3.4 Aethalometer

307 The concentration of equivalent black carbon (eBC) in the PM₁ size range was measured by using two different Magee
308 Scientific Aethalometer models: AE–31 during 2012–2017, and AE–33 in 2018. The sample air was taken through an
309 inlet equipped with a PM₁₀ cyclone and a Nafion dryer, and a PM₁ impactor. Aethalometers determine the concentration
310 of eBC by collecting aerosols on a filter medium and measuring the change in light attenuation through the filter. Both of
311 the Aethalometers quantify eBC concentration optically at seven wavelengths (370, 470, 520, 590, 660, 880 and 950 nm).
312 Only the eBC concentration determined at 880 nm was used in the current study. AE–31 data was corrected for a filter
313 loading error with a correction algorithm derived previously (Collaud Coen et al., 2013). A mass absorption cross section
314 of 4.78 m² g⁻¹ at 880 nm was used in the eBC concentration calculation. The AE–33 used a “dual-spot” correction is
315 described previously (Drinovec et al., 2015).

316 2.3.5 OCEC–analyser

317 Organic carbon (OC) and elemental carbon (EC) concentrations were measured using a semi-continuous Sunset OCEC
318 analyser (Bauer et al., 2009) produced by Sunset Laboratories Inc. (USA). The aerosol sampling was conducted through
319 the same container roof as the ACSM. The inlet length was approximately the same as for the ACSM (ca. 3 m). The
320 sample flow was guided through a PM_{2.5} cyclone and a carbon plate denuder to avoid collection of large particles and a

321 positive artefact introduced by organic vapours. In the OCEC, the sample is collected on a quartz-filter for 2.5 hours with
322 an 8 Lpm flow rate. The sampling procedure is followed by the analysis phase. The analysis phase includes thermal
323 desorption of PM from the filter following the EUSAAR-2 protocol (Cavalli et al., 2010), and introducing the aerosol
324 sample to inert helium gas that is used to carry the OC to a MnO₂ oxidising oven. This leads to OC oxidation to CO₂,
325 which is then quantified, with a non-dispersive infrared (NDIR) detector. Afterwards the remaining sample is introduced
326 to a mixture of oxygen and helium enabling EC transfer to the oven. The resulting CO₂ from EC desorption and
327 combustion is also quantified using the NDIR detector. An additional optical correction was used to account for the
328 amount of pyrolysed OC during the helium phase. EC was also quantified using a laser installed in the analyser. This
329 method is similar to the Aethalometer (see [chapter 2.3.4 Aethalometer](#)). After each analysis phase, a calibration cycle was
330 performed via methane oxidation. The instrument was maintained extensively in November 2017, thus making the year
331 2018 most reliable for ACSM comparison. Only data measured in 2018 was used in this study.

332 **2.3.6 MARGA-2S**

333 Inorganic gases (HCl, HNO₃, HONO, NH₃, SO₂) and major inorganic ions in PM_{2.5} and PM₁₀ fraction (Cl⁻, NO₃⁻, SO₄²⁻,
334 NH₄⁺, Na⁺, K⁺, Mg²⁺, Ca²⁺) were measured with one hour time-resolution using the online ion chromatograph MARGA
335 2S ADI 2080 (Applikon Analytical BV, Netherlands). In the MARGA instrument, ambient air was taken through the inlet
336 to a wet rotating denuder where the gases were diffused in absorption solution (10 p.p.m hydrogen peroxide). Aerosol
337 particles that passed through denuder were collected in a steam jet aerosol collector. The sample solutions from the
338 denuder as well as the steam jet aerosol collector were collected in syringes and injected in an anion and cation ion
339 chromatograph with an internal standard solution (LiBr). Cations were separated in a Metrosep C4 (100/4.0) cation
340 column using 3.2 mmol L⁻¹ MSA eluent. For anions, a Metrosep A Supp 10 (75/4.0) column with Na₂CO₃ – NaHCO₃ (7
341 mmol L⁻¹ / 8 mmol L⁻¹) eluent were used. The detection limits for all the components were 0.1 µg m⁻³, or smaller. The
342 unit used for the current study is described in more detail previously (Makkonen et al., 2012).

343 **2.4 ACSM collection efficiency correction**

344 [The ACSM data processing includes correcting for the measurement collection efficiency \(CE\) that is estimated to be](#)
345 [approximately 0.45–0.5 in average for AMS-type instruments \(Middlebrook et al., 2012\).](#) The reduction is caused by
346 particle bouncing at the instrument vaporizer (Middlebrook et al., 2012). Middlebrook et al. (2012) provide a method to
347 estimate the CE, based on aerosol chemical composition. However, this method was not applicable to our data set due to
348 low, and thus noisy, ammonium signals that were most of the time near the instrument detection limit. Thus, we chose to
349 calculate the collection efficiency based on the ratio between the NR-PM₁ (total mass concentration measured by the
350 ACSM) and a Differential Mobility Particle Sizer (DMPS)-derived mass concentration (after subtracting the equivalent
351 black carbon, eBC). [The DMPS-derived mass concentration is determined as follows: 1\) Calculation of aerosol volume](#)
352 [concentration \(m³ m⁻³\) of the ACSM detectable size range, where the aerodynamics lens transmission is most efficient](#)
353 [\(50–450 nm in electrical mobility = ~75–650 nm in vacuum aerodynamic diameter\) and assuming spherical particles, 2\)](#)
354 [Estimating aerosol density based on the ACSM-measured chemical composition \(\$\rho_{\(\text{NH}_4\)_2\text{SO}_4} = 1.77 \text{ g cm}^{-3}\$, \$\rho_{\text{NH}_4\text{NO}_3} = 1.72\$](#)
355 [g cm⁻³, \$\rho_{\text{org}} = 1.50 \text{ g cm}^{-3}\$, \$\rho_{\text{BC}} = 1.00 \text{ g cm}^{-3}\$ \), 3\) Calculating the mass concentration \(µg m⁻³; mass concentration = density](#)
356 [× volume concentration\). As direct scaling of ACSM data to the DMPS-derived and eBC subtracted mass concentration](#)
357 [is strongly not recommended, we chose to use two-month running medians of the ratio between the NR-PM₁ and eBC-](#)
358 [subtracted DMPS-derived mass concentration. The two-month running median approach diminishes the effect instrument](#)

359 noise in the DMPS-derived mass concentration that could otherwise be introduced as additional uncertainty into the
360 ACSM-data. The two-month median CEs were within 10% of the annual mean values in years 2013–2018. In 2012 the
361 CE had stronger seasonal variation (16% variation around the mean, peaking in summer) likely due to the lack of the
362 aerosol dryer in the sampling line. The magnitudes of the CEs can be obtained from [Figure 2a](#).

363
364 [Figure 2a](#) depicts the linear regression fits for ACSM mass concentration (without CE correction) and eBC-subtracted
365 DMPS-derived mass concentration scatter plots for each year. The correlation coefficients (Pearson R^2) between these
366 two independently measured variables are high, indicating that both ACSM and DMPS functioned well throughout the
367 long dataset. Years 2012, 2016–2018 have linear regression fit slopes (k) corresponding to CE values reported in the
368 literature (Middlebrook et al., 2012), whereas slopes for years 2013–2015 were higher than expected. The most likely
369 reason for these high values were calibration difficulties that might have led to underestimation of the instrument RF_{NO_3}
370 that is required in the mass concentration calculation. This possible RF_{NO_3} underestimation was accounted for in the
371 DMPS-based CE correction with higher CE values than theoretically suggested for ACSM-systems. The resulting
372 agreement between the eBC-subtracted DMPS-derived mass concentration and the CE corrected ACSM-derived mass
373 concentration is presented in [Figure 2b](#). As the NR- PM_1 incorporates the two-month running median of the CE calculated
374 using DMPS-data, it is not surprising that a good correlation was achieved.

375
376 [Figures 2c&d](#) visualise the relationship between ACSM-derived mass concentration and a Dekati impactor PM_1 data
377 (see 2.3.2 Cascade impactor for instrument description) before and after CE correction, respectively. The impactor PM_1
378 is not eBC subtracted as it would have significantly decreased the number of points in the analysis. The degree of
379 agreement between the ACSM and impactor measurements is significantly lower compared to the agreement between the
380 ACSM and DMPS. The reason for this is likely the fact that the Dekati impactor measurements are prone to uncertainties
381 due to long sampling times and manual weighing. This scatter is reduced slightly in [Figure 2d](#) compared to [Figure 2c](#) due
382 to the DMPS-based CE correction and the slope-values (k) increase. As the agreement between the ACSM-derived mass
383 concentration and impactor PM_1 is better after CE correction both due to increased correlation coefficients (R^2) and slopes
384 (k), the (two month running median) DMPS-based CE correction is justified. Hereafter, all the ACSM data presented and
385 discussed are CE corrected. We refer to it as NR- PM_1 . The CE correction method applied importantly also [ensures](#) more
386 quantitative year-to-year comparability of the ACSM data acquired as it also corrected for the overestimated calibration
387 values obtained during 2013–2015.

388 2.5 ACSM chemical speciation validation

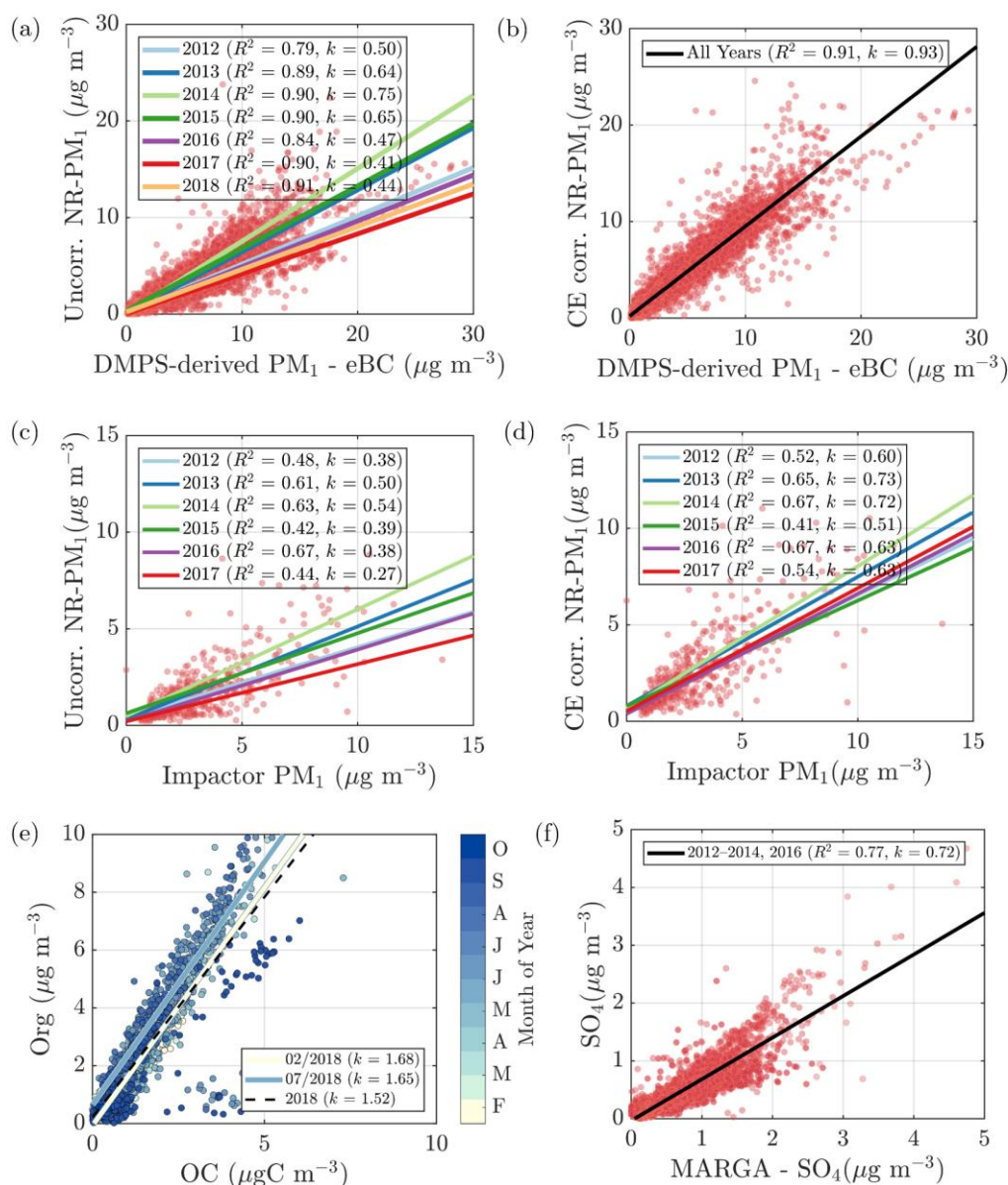
389 To validate the ACSM chemical speciation process, the ACSM organics (Org) and sulphate (SO_4) were compared against
390 the organic carbon (OC) measured by a Sunset OCEC-analyser (see section 2.3.5 OCEC-analyser for instrument) ([Figure](#)
391 [2e](#)) and water-soluble sulphate measured by a MARGA-2S (see section 2.3.5 MARGA-2S for instrument description)
392 ([Figure 2f](#)), respectively. Both of these reference instruments sample the $PM_{2.5}$ range, and thus we expect them to detect
393 also larger particles and thus a higher mass loading than the ACSM, when particles exceeding $1 \mu m$ in aerodynamic
394 diameter are present in the ambient air. The OC and Org measurements show a high degree of agreement indicated by
395 Pearson R^2 of 0.72 during the overlapping measurement period at SMEAR II. The slope of the linear regression fit ($k =$
396 [1.52](#)) is comparable to literature values of organic matter to organic carbon ratios (OM:OC) (Turpin and Lim, 2001; Lim
397 and Turpin, 2002; Russell, 2003). The linear regression is calculated using all the overlapping data from year 2018, when

398 the OCEC was well functioning after instrument service. Regarding the water-soluble inorganic ions, only the SO_4^{2-}
399 concentration (in $\text{PM}_{2.5}$), retrieved from the MARGA measurements, was used for the current analysis for ACSM data
400 validation purposes. The nitrate time series, for example, are known to be different between the two measurements at
401 SMEAR II (Makkonen et al., 2014). The scatter between the nitrate measurements, visualised also here, in Figure A.3,
402 could serve as evidence of organic nitrates, which are not efficiently detected by MARGA (Makkonen et al., 2014). The
403 presence of organic nitrates are discussed later in the manuscript (see chapter 3.2 Diurnal variation of NR-PM_1
404 composition). Other factors influencing the nitrate agreement could arise from the MARGA nitrate background
405 subtraction procedure, the overall low nitrate signal at SMEAR II (Makkonen et al., 2014), an organic CH_2O^+ fragment
406 coinciding with NO^+ at m/Q 30 Th leading to ACSM nitrate over prediction under certain conditions, and the difference
407 between the ACSM and MARGA size cuts (PM_1 vs $\text{PM}_{2.5}$). The ACSM sulphate, however, correlates well with MARGA
408 (Pearson $R^2 = 0.77$), but has a slightly lower Pearson R^2 compared to an earlier < 11-month MARGA vs AMS comparison
409 from SMEAR II (Pearson $R^2 = 0.91$) (Makkonen et al., 2014). Overall, based on the good agreement between ACSM and
410 Sunset OCEC, MARGA, DMPS and Dekati cascade impactor measurements, we are confident of the year-to-year
411 comparability of our ACSM dataset.

412

413

414



415

416 **Figure 2** (Panel a) The NR-PM₁ mass concentration without collection efficiency (CE) correction vs the DMPS-derived eBC
 417 subtracted mass concentration. The linear fits are displayed with solid lines for each year, respectively. The slopes of the linear fits (k)
 418 and Pearson correlation coefficients (R^2) are presented in the figure legend. (Panel b) CE-corrected NR-PM₁ mass concentration vs
 419 the DMPS-derived eBC subtracted mass concentration. The black line represents the overall linear fit. (Panel c) The NR-PM₁ mass
 420 concentration without collection efficiency (CE) correction vs the Dekati impactor PM₁ concentration. The linear fits are displayed
 421 with solid lines for each year, respectively. (Panel d) CE-corrected NR-PM₁ mass concentration vs correction vs the Dekati impactor
 422 PM₁ concentration. The linear fits are displayed with solid lines for each year, respectively. (Panel e) The ACSM organics vs the PM_{2.5}
 423 organic carbon (OC) detected with a semi-continuous OC/EC analyser. The black dashed line represents the overall linear fit (Pearson
 424 $R^2 = 0.72$), and the solid white and blue linear fit lines represent the February and July fits, respectively. The color coding indicates
 425 the month of the year in 2018. (Panel f) The ACSM sulphate vs the PM_{2.5} sulphate detected with MARGA-2S. The black line represents
 426 the overall linear fit. In all of the panels, red dots represent all the measurement points collected in the course of the measurement
 427 period.

428

429 **2.6 Openair polar plots with ZeFir pollution tracker**

430 The wind direction dependence of different NR-PM₁ chemical species observed at SMEAR II were investigated with
431 openair bivariate polar plots. Openair is an open source, R-based package described previously (Carslaw and Ropkins,
432 2012). Briefly, the openair polar plots show how the pollutant concentration varies under different wind speed and
433 direction. The calculation of the polar plots are based on binning pollutant concentration data into different wind direction
434 and speed bins followed by the concentration field interpolation. As the polar plots do not take the frequencies of the wind
435 direction nor wind speed into account, they should be investigated together with a traditional wind rose representing the
436 likelihood of each wind direction and wind speed combination. The ZeFir pollution tracker (Petit et al., 2017), an Igor
437 Pro (Wavemetrics Inc, USA) based graphical interface for producing openair polar plots among other functionalities, was
438 utilized in the current study. Median statistics with fine resolution were set in the ZeFir-based openair initialisation. These
439 plots provide an informative first step for tracking PM₁ and its precursors' wind direction and speed dependence.

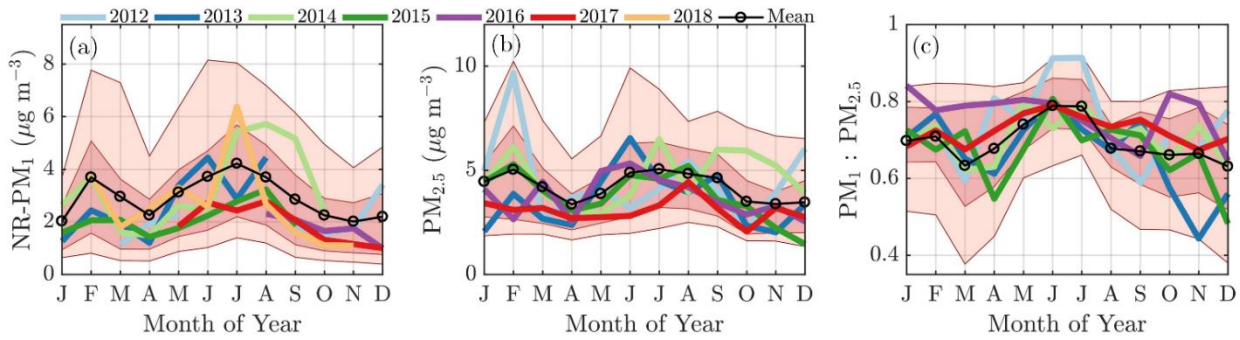
440 **3 Results and discussion**

441 First, we state that the ACSM data set was not long enough to provide sufficient statistics for investigation of long-term
442 trends of NR-PM₁ or its components' loading, hence no analysis of such is presented here. In this section we discuss the
443 inter- and intra-annual variation in sub-micron non-refractory aerosol chemical composition at SMEAR II in 2012–
444 2018. We first introduce the monthly scale behaviour and year-to-year variability. We briefly introduce two case studies,
445 one linked to elevated sulphate loading at the station due to a lava field eruption in Iceland, and another one discussing
446 the effect of heatwaves on PM₁ loading and composition. Hereafter, we introduce the overall median diurnal profiles of
447 individual chemical species observed in the NR-PM₁, and finally the chemical composition observations linked to wind
448 speed and direction observations above the forest canopy.

449 **3.1 Inter- and intra-annual variation**

450 The monthly median seasonal cycles of NR-PM₁ and PM_{2.5} show bimodal distributions as the PM loading has two
451 maxima: one peak in February, and another one in summer (June, July, and August), the latter one being more significant.
452 This can be observed from [Figures 3a&b](#), where the monthly median PM loading for each year is visualised. The NR-
453 PM₁ seasonal cycle ([Figure 3a](#)) is more pronounced compared to the PM_{2.5} cycle ([Figure 3b](#)). A possible reason for this
454 could be the lack of PM_{2.5} data in 2018 that is having a high impact on the NR-PM₁ July peak. The PM₁/PM_{2.5} ratio
455 ([Figure 3c](#)) in turn, calculated using the Dekati Impactor data alone, demonstrates that most of the time, 60–80% of PM_{2.5}
456 can be explained by PM₁. The ratio is lowest (60–70%) in wintertime (December, January, February) implying an
457 increased mass fraction of particles with aerodynamic diameters greater than a micrometre, compared to the summertime,
458 when the ratio is nearly 80%.

459



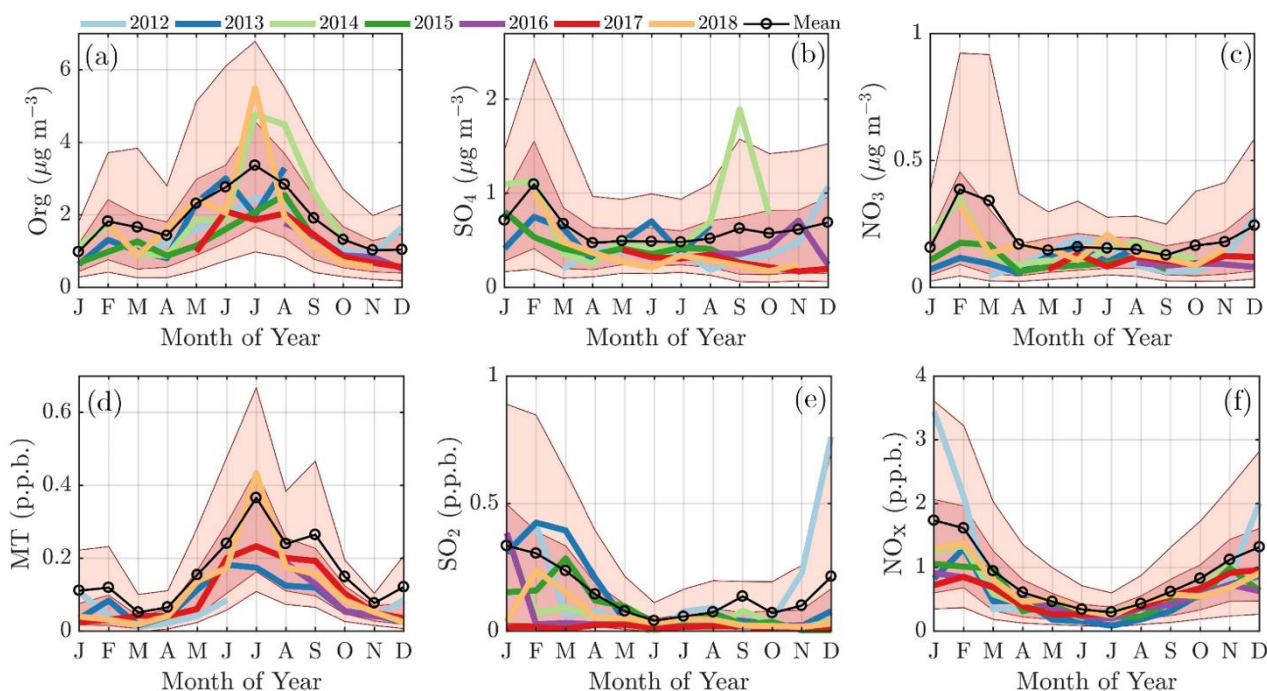
460

461 **Figure 3** The monthly cycles of NR-PM₁ (Panel a), PM_{2.5} (Panel b), and the ratio between PM₁ and PM_{2.5} (Panel c). The median
 462 monthly values for each year are individually displayed with the coloured solid lines. The black circled line represents the overall
 463 monthly mean values. The dark red shaded area is drawn between the overall 25th and 75th percentiles and the lighter red shaded area
 464 between the overall 10th and 90th percentile. The x-axes represent the time of the year and the y-axes in panels a and b mass
 465 concentration in $\mu\text{g m}^{-3}$ and a unit less ratio in panel c.

466

467 The February PM maximum is linked to an enhanced loading of inorganic aerosol species, such as nitrate and especially
 468 sulphate, as well as a slight increase of organics (Figures 4a-c), whereas the summertime maximum is explained by a
 469 massive enhancement of organics alone (Figure 4a). The main precursors for inorganic aerosols, i.e. SO₂ and NO_x peak
 470 during winter albeit less sharply on February alone (Figure 4e&f). As fossil fuel combustion processes are the major
 471 sources of SO₂ and NO_x, their emissions likely increase during cold months due to enhanced need for residential heating,
 472 for example. More importantly, these emissions are trapped in a shallow atmospheric boundary layer increasing the
 473 concentration recorded within it. One possible reason for the “lack” of sulphate and nitrate aerosol outside February,
 474 despite the great availability of SO₂ and NO_x, is likely related to wind direction transitioning, discussed later in the
 475 manuscript. Another effect could be the darkness prohibiting photochemistry needed for inorganic aerosol formation.
 476 Indeed, the global radiation measured above the forest canopy shows only a minimal short wave radiation flux in
 477 November, December and early January, but it increases mid-January onwards (Figure 1b). As February is generally
 478 drier (in terms of less precipitation) than the other winter months (Pirinen et al., 2012), the lifetime of aerosols could be
 479 greater, making the inorganic particles more likely to reach SMEAR II. The inorganic nitrate (ammonium nitrate)
 480 formation is highly dependent on ammonia availability. The ammonia concentration during wintertime is nearly
 481 negligible at SMEAR II and increases rapidly in spring (Makkonen et al., 2014). The low nearby ammonia availability
 482 suggests that the wintertime nitrate is long-range transport.

483



484

485 **Figure 4** The monthly cycles of organics (panel a), sulphate (panel b) and nitrate (panel c) concentrations in the NR-PM₁, and their
 486 major precursors, i.e. monoterpenes (panel d), sulphur dioxide (panel e), and nitrogen oxides (panel f). The median monthly
 487 concentrations for each year are individually displayed with the coloured solid lines. The black circled line represents the overall
 488 monthly mean values. The dark red shaded area is drawn between the overall 25th and 75th percentile and the lighter red shaded area
 489 between the overall 10th and 90th percentile. The x-axes represent the time of the year and the y-axes in panels a–c mass concentration
 490 in $\mu\text{g m}^{-3}$, and d–f in parts per billion (p.p.b.).

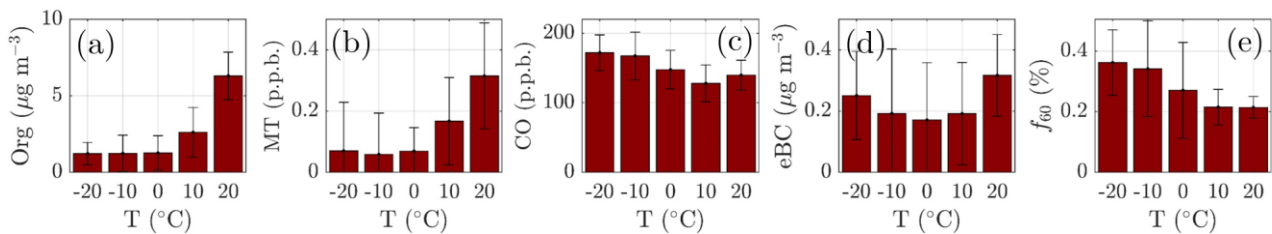
491

492 Monoterpenes also show a non-zero loading during all winter months (Figure 4d). Their source is likely anthropogenic,
 493 such as the nearby sawmills, rather than biogenic due to the low ambient temperature limiting their biogenic emissions
 494 (Guenther et al., 1993; Hakola et al., 2012; Kontkanen et al., 2016). Their wintertime presence could be linked to their
 495 overall decreased photochemical sink and them being emitted to the shallower atmospheric boundary layer with little
 496 vertical dilution. The monoterpene mixing ratio starts increasing rapidly in April achieving its maximum monthly median
 497 value during July (Figure 4d), simultaneously with NR-PM₁ organics (Figure 4a). Previous studies have shown that
 498 monoterpene emissions increase exponentially with ambient temperature (Guenther et al., 1993; Aalto et al., 2015). As
 499 the current study does not incorporate monoterpene emission data, we visualise the behaviour of monoterpene mixing
 500 ratio with increasing ambient temperature in Figure 5b. The increase in monoterpene mixing ratio is likely a combined
 501 result from increased biological plant activity in the forest as well as the increased emissions due to higher temperature.
 502 Organic aerosol concentration behaves in a similar manner as a function of temperature, as depicted in Figure 5a. Such
 503 behaviour in organic aerosol loading is often attributed to biogenic SOA formation from BVOCs (Daellenbach et al.,
 504 2017; Stefenelli et al., 2019; Vlachou et al., 2018; Paasonen et al., 2013).

505

506 Besides biogenic SOA, also open fire biomass burning organic aerosol (BBOA) is a major contributor to summertime
 507 organics worldwide, from wild fires during dry conditions (Bond et al., 2004; De Gouw and Jimenez, 2009; Mikhailov et
 508 al., 2017; Corrigan et al., 2013). An enhancement in eBC concentration, a tracer for BBOA, was observed as a function
 509 of temperature at SMEAR II implying the possible presence of BBOA in the summertime sub-micron aerosol (Figure

510 5d). However, uncertainties can be attributed to the eBC concentration as scattering coatings, such as salts or even
 511 photochemically aged SOA can also generate a lensing effect leading to an overestimation of eBC (Bond and Bergstrom,
 512 2006;Zhang et al., 2018). Such effect could lead to a substantial overestimation of eBC especially in summertime, when
 513 the organic loading is highest. Some certainty of the BBOA and BC enhancement with high temperatures can however
 514 be retrieved from Figure 5c, where carbon monoxide (CO) mixing ratio also increases at relatively high ambient
 515 temperatures ($T > 15\text{ }^{\circ}\text{C}$). CO is known to be emitted from incomplete combustion processes. Nonetheless, as the increase
 516 in eBC visualised in Figure 5d is less drastic than for monoterpenes, we suggest the biogenic SOA production as the major
 517 organic aerosol source in summertime. While the quantification and separation of BBOA from SOA will be the topic of
 518 an upcoming independent publication centred on the analysis of organic aerosol mass spectral fingerprints at SMEAR II,
 519 we briefly introduce the behaviour of f_{60} . f_{60} , which equals the contribution of m/Q 60 Th signal to the total organic signal
 520 recorded by the ACSM, is a marker for levoglucosan-like species originating from cellulose pyrolysis in biomass burning
 521 (Schneider et al., 2006;Alfarra et al., 2007). f_{60} is present at high percentages in fresh BBOA plumes (Cubison et al.,
 522 2011), but decays due to BBOA photochemical aging into oxidised organic aerosol. The fairly rapid (in order of several
 523 hours to days) photochemical aging of BBOA has been a topic of earlier chamber (Grieshop et al., 2009;Jimenez et al.,
 524 2009) and ambient studies (DeCarlo et al., 2010;Cubison et al., 2011). Here, unlike CO and eBC, f_{60} does not increase as
 525 a function of temperature in the highest temperature bins, but stays rather constant albeit lower than the f_{60} values recorded
 526 under cold temperatures at SMEAR II (Figure 5e). As the possible wild fires contributing to SMEAR II CO and eBC
 527 under high ambient temperatures also occur further away, it is likely that the BBOA is oxidised before detected at SMEAR
 528 II. CO and eBC can be considered as more inert BBOA markers compared to f_{60} . The wintertime f_{60} is likely linked to
 529 wintertime biomass burning (for domestic heating purposes) emissions trapped in the shallow mixing layer. These
 530 emissions are discussed more later on in the manuscript (see chapter 3.2 Diurnal variation of NR-PM₁ composition).”
 531



532
533

534 **Figure 5** The daily mean organic aerosol (Org, panel a), monoterpene (MT, panel b), carbon monoxide (CO, panel c), equivalent
 535 black carbon (eBC, panel d) concentrations, and the fraction of the ACSM Org-signal made up by levoglucosan-like species (f_{60} , panel
 536 e) recorded under different ambient temperatures. The values recorded assigned into 10 °C wide bins based on the daily ambient
 537 temperature mean. The marker error bars show the standard deviation of the values in each bin.

538

539 3.1.1 Case study: The effect of warm summers on organic aerosol loading

540 The highest NR-PM₁ mass concentrations were detected during summers of 2014 and 2018. These summers were the
 541 hottest during the whole measurement period (Figure 6a), and linked to persistent high pressure conditions (Sinclair et
 542 al., 2019;FMI, 2014) . The non-parametric probability densities (Kernel distributions) for temperature for July 2012–
 543 2018, displayed individually in Figure 4a, show clearly higher temperatures in July 2014 and 2018. Indeed, these months
 544 were abnormally warm as July 2014 was 2.2°C, and July 2018 was 3.4°C higher than the 7-year July mean (16.6 °C).
 545 Comparing to the 30-year July climate at SMEAR II (1981–2010) (Pirinen et al., 2012), the mean temperature in July

546 2014 was 2.8°C, and July 2018 4.0°C higher. As can be seen from Figures 4a&d, both organic aerosol and monoterpene
547 concentration positively responded to this temperature change with high median values. The same phenomenon is
548 visualised in Figures 4b&c through Kernel densities for particulate organics and monoterpenes, respectively, for July of
549 each year. The recorded organic aerosol concentration was 50% higher than the 7-year mean in July 2014, and 70%
550 higher in 2018. The monoterpene concentration in turn was 50% higher in 2018 compared to the mean of all available
551 July data (due to PTR-MS sensitivity issues, the 2014 data was chosen to be excluded from the analysis).

552
553 As the high-pressure weather ruling in Julys 2014 and 2018 further promoted clear-sky conditions, also the oxidation
554 capacity of the air was likely affected. This could have led to efficient monoterpene oxidation towards condensable low-
555 volatility products. Furthermore, their condensation onto particles could explain the observed high organic aerosol mass
556 concentration. The SOA formation enhancement as a function of temperature has also been investigated previously in a
557 modelling study, where a significant global increase in monoterpene-derived organic aerosol concentration was projected
558 to future, following different climate scenarios introduced by the Intergovernmental Panel of Climate Change (IPCC)
559 (Heald et al., 2008). Kourtchev et al. (2016) investigated the effect of high ambient temperature on biogenic SOA loading
560 and composition utilising measurement data from SMEAR II. They include summers 2011 and 2014 to their analysis,
561 where 2011 summer represents a significantly colder summer (average ambient temperature was 8°C less than in 2014).
562 By utilising ultra-high resolution off-line mass spectrometry on filter samples collected at SMEAR II, they detected a
563 significantly higher SOA oligomer content during 2014. Their results not only highlight the large increase in SOA mass
564 as a function of temperature, but also on the SOA composition differences affected by the large SOA content which
565 further influenced the CCN formation potential of SOA.

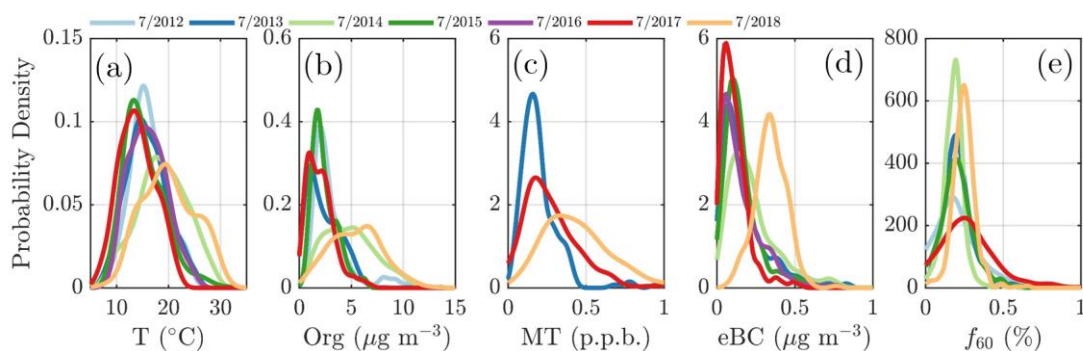
566
567 A quick revisit to the OCEC vs ACSM comparison performed earlier in the manuscript (Figure 2e) shows relatively high
568 Org/OC-values ($k = 1.68$) for July 2018, which further indicates of high oxygenation of OA (Aiken et al., 2008). However,
569 the time series of the ruling monthly Org/OC-values, visualised in Figure A.5, reveal an even higher Org/OC for August
570 2018. Further analysis of Org/OC recorded from SMEAR II is needed to answer whether such behaviour is frequently
571 occurring at SMEAR II, or whether July 2018 organic aerosol was less functionalised (oxidised) than usual due to higher
572 presence of primary organic aerosol, such as BBOA, than usual. Thus, not to link the organic aerosol increase to biogenic
573 SOA formation exclusively, we also investigated the presence of BBOA in the sub-micron aerosol during Julys 2014 and
574 2018 via Kernel distributions for eBC and f_{60} , presented in Figure 6d&e. The eBC distribution clearly hints towards
575 BBOA presence during July 2018, whereas July 2014 seems much less affected. Importantly, we also want to inform that
576 in July 2018 we had only one week of eBC data available. The July 2018 eBC could be linked to the severe wild fires
577 occurring in Sweden during July and August 2018. The July eBC measurement period overlaps with the forest fire
578 occurrence period. Sweden also suffered from wild fires in August 2014, not depicted in Figure 6 that focuses on Julys
579 alone. The f_{60} in turn follows the conclusions made earlier in the context of Figure 5 as the f_{60} values remain low each
580 July, and approach the f_{60} background levels of 0.3% (Cubison et al., 2011; Figure 6e). Importantly, such negligible f_{60}
581 signals were detected under the influence of an aged BBOA plume originating from Moscow and Northern Ukraine wild
582 fires at SMEAR II also in 2010 (Corrigan et al., 2013). An AMS, which was used as one of the measurement tools in the
583 campaign, detected mass spectra resembling oxidised organic aerosol during the biomass burning influence. These data
584 correlated well with multiple biomass burning markers including CO, potassium and acetonitrile despite the lack of
585 resemblance with fresh BBOA mass spectra with high f_{60} . Corrigan et al. (2013) finally attributed up to 25% of the organic

586 aerosol to BBOA originating from the Moscow and Northern Ukraine wild fires. 35% of the organic aerosol mass was
587 associated with biogenic SOA formation. The weather during the Corrigan et al. (2013) study period in 2010 was also
588 unusually warm ($T_{\text{avg}} = 20^{\circ}\text{C}$), and resembled summers 2014 and 2018 regarding the ruling anti-cyclonic circulation
589 pattern.

590

591 The frequency, duration and intensity of heatwaves are projected to increase in the future Finnish climate due to positive
592 pressure anomalies over Finland and to the east of Finland, as well as a negative pressure anomaly over Russia between
593 90 and 120°E (Kim et al., 2018). Moreover, the IPCC states that droughts and insect outbreaks, are projected to be boosted
594 in the warming climate (Barros et al., 2014). Recent findings by Zhao et al. (2017) show how such biotic and abiotic
595 stress factors enhance VOC emissions from plants that further contribute to organic aerosol after oxidation (Zhao et al.,
596 2017). Wildfires in turn are likewise likely to occur globally more frequently in the future due to increasing number of
597 long-lasting heatwaves (Spracklen et al., 2009). Indeed, BBOA loadings due to wildfires already show a slight increase
598 in the United States (Ridley et al., 2018). Based on these previous studies, as well as our observations together with the
599 Corrigan et al. (2013) study from SMEAR II, the increasing frequency of heat waves and wildfires will enhance the
600 particulate matter loading at SMEAR II in the future, and continuous long-term measurements, like the ones presented
601 here, will be important in monitoring such changes.

602



603

604 **Figure 6** Non-parametric probability densities (Kernel distributions) of temperature (panel a), organic aerosol (panel b), monoterpenes
605 (panel c), equivalent black carbon (panel d) concentrations, and the fraction of the ACSM organic signal made up by levoglucosan-
606 like species (f_{60} ; panel e) during individual Julys across the measurement period (2012–2018). The data availability for eBC was one
607 week in July 2018. The x-axes represent the T, Org, MT and eBC values recorded, respectively and the y-axes the non-parametric
608 probability densities. Briefly, the Kernel distributions are similar to smoothed histograms of the measurement data. This visualisation
609 was chosen to avoid assumptions of the nature of distribution that might hide important features of the measurement data if presented
610 with normal distributions, for instance.

611

612 3.1.2 Case study: Sulphate transport from Holuhraun flood lava eruption

613 The sulphate loading in September 2014 represents the largest outlier in Figure 4b with the average mass concentration
614 five times greater than the overall September mean. The mean SO_2 concentration during September 2014 was 0.66 p.p.b.,
615 which is 0.50 p.p.b. higher than the mean SO_2 mixing ratio representing all the Septembers during the measurement period
616 (0.16 p.p.b.). The elevated median SO_2 concentration during September 2014 is also visible in Figure 4e. To investigate
617 the source of sulphur, we displayed the full atmospheric column SO_2 concentration during September 2014 utilising
618 satellite observations (Figure A.6a). The SO_2 concentration hot spot was located in Iceland and is linked to the fissure
619 Bárðarbunga–Veidivötn eruption at Holuhraun (Aug 31st 2014 – Feb 28th 2015) that yielded 20–120 kilotons a day of SO_2
620 (Schmidt et al., 2015). The concentration above SMEAR II was obviously not comparable to the loading near the eruption

621 site. However, based on a rough trajectory analysis (Figure A.6b) we link our observations of elevated sulphate and SO₂
622 during September 2014 to the diluted plume from Holuhraun.

623 3.2 Diurnal variation of NR-PM₁ composition

624 The year-to-year variation in the NR-PM₁ monthly median seasonal cycles shows rather consistent behaviour throughout
625 the measurement period and even the overall 10th percentile of the PM-data suits the bimodal trend discussed in the
626 section above. The 10th percentile also agrees with the seasonal trends associated with individual NR-PM₁ chemical
627 species, i.e. organics, sulphate and nitrate as well as their precursors (Figure 4). Few outliers observed are discussed in
628 the chapters above (see chapters 3.1.1 Case study: The effect of warm summers on organic aerosol loading and chapter
629 3.1.2 Sulphate transport from Holuhraun flood lava eruption). As the year-to-year variability between different years is
630 rather minimal, we decided to investigate the overall median temporal behaviour of aerosol chemical composition further
631 via Figure 7. The subplots in this figure are based on data matrices of median diurnal cycles (1h resolution) for every two
632 weeks of a year (24 × 26 matrix). The matrices are visualised with contour plots (*contourf*, MATLAB 2017a) except for
633 Figure 7h, due to the high noise level of the time trace.

634
635 Neither the NR-PM₁ concentration nor its chemical species have large diurnal variability during wintertime (Figure 7a)
636 due to low solar radiation and the lack of diurnal variability in ambient temperature (Figures 1a&b) prolonging the life
637 time of aerosols. Thus, the wintertime chemical composition of NR-PM₁ stays stable over the course of the day (Figures
638 7b&d). As wintertime PM is presumably mostly long-range transport, its components' diurnal patterns are less obvious
639 due their cumulative build-up in the atmosphere. For example, as sulphate aerosols, the most prominent inorganic species,
640 are long lived due to their low volatility, we do not expect sulphate to have diurnal variation in wintertime because of the
641 lack of major SO₂ sources at SMEAR II's proximity. The ammonium mass concentration lacks diurnal pattern as well
642 and peaks at the same time of the year as sulphate. The degree of aerosol neutralisation by ammonia can be estimated by
643 the ratio between the measured ammonium and the amount of ammonium needed to neutralise the anions detected by the
644 ACSM (termed "NH₄ predicted") (Zhang et al., 2007b). The overall ratio was 0.66 hinting towards moderately acidic
645 ammonium sulphate aerosols (Figure A.7&Figure 7h), though the uncertainty in this value is high due to the low loadings
646 of ammonium at SMEAR II. We also acknowledge that the ratio between measured and predicted ammonium
647 concentration is not fully accurate for acidity estimations, and if such are needed, a better estimation could be provided
648 with thermodynamic models. The temporal variation of the ammonium balance does not show diurnal variability either,
649 but a very modest decrease during January (Figure 7h), when the ambient temperature was the lowest. In the case of
650 wintertime organic aerosol, the lack of a diurnal trend (Figure 7c) indicates that nearby residential heating (expected
651 mainly in evenings) emissions are not a dominating source of organics at the site despite their clear presence in the
652 wintertime aerosol as depicted by the seasonal *f₅₀* trend depicted in Figure A.4. In general, the lack of a distinct diurnal
653 pattern rather hints towards long-range transported organics. Such conclusions can also be made based on the rather high
654 Org/OC linear regression slope for February data (*k* = 1.65) depicted in Figure 2e (see also Figure A.5). As mentioned
655 earlier, a high Org/OC-ratio indicates a higher degree of functionalisation/oxidation of organic aerosol (Aiken et al.,
656 2008).

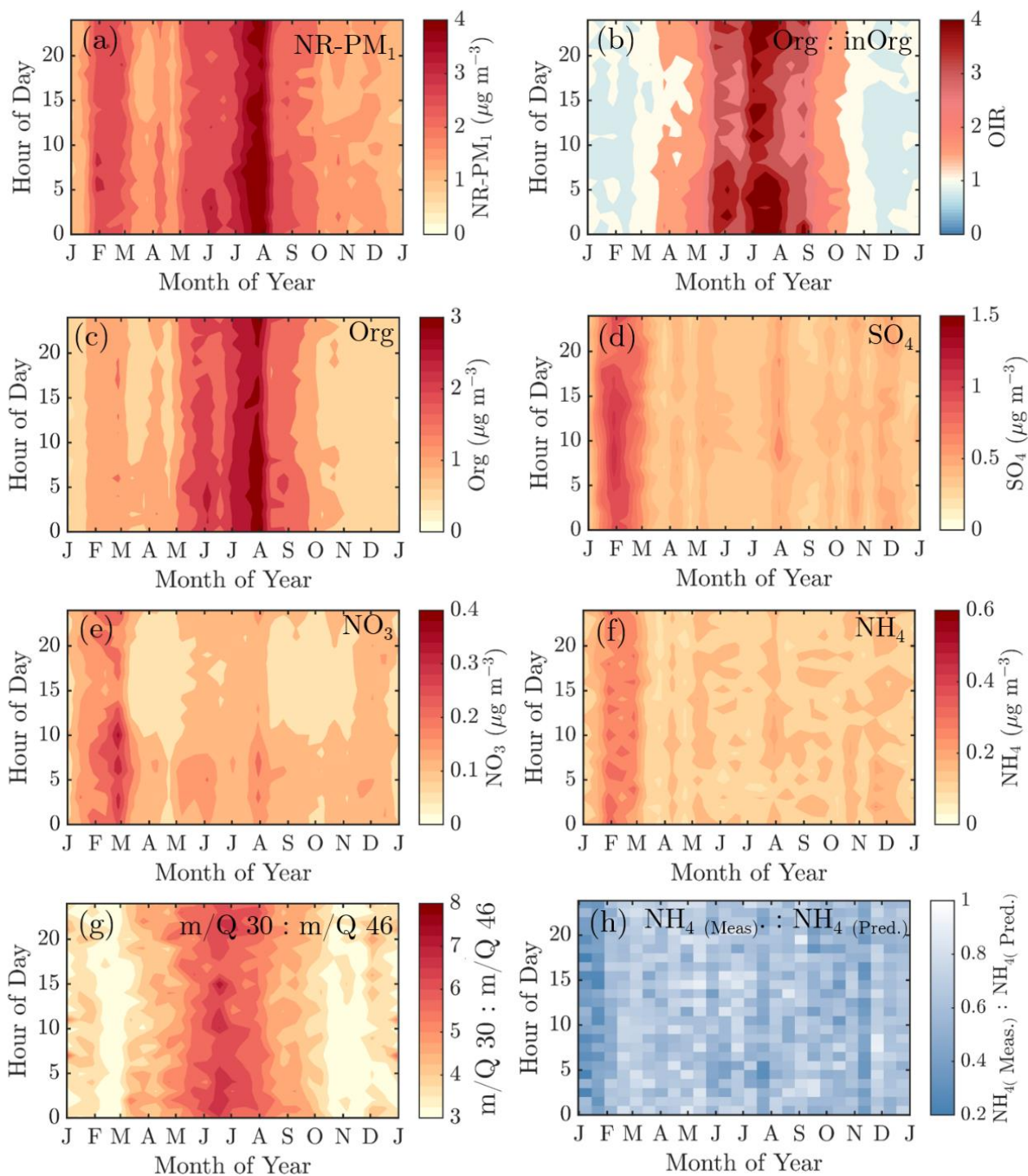
657
658 From March onwards, when the solar radiation flux has significantly increased, the aerosol chemical composition starts
659 to show modest diurnal variability. The ratio between organic and inorganic aerosol chemical species (OIR) exhibits

660 diurnal variability from March to October, when also ambient temperature has strong diurnal variation. The OIR achieves
661 its minimum during daytime and maximum during night (Figure 7b). In other words, particles have the highest organic
662 fraction during night-time and early mornings. The organic aerosol mass concentration increases during night (Figure 7c),
663 likely due to more efficient partitioning of semi-volatile species into the aerosol phase. This effect is seen even more
664 clearly in the nitrate concentration (Figure 7e), with a strong diurnal pattern largely tracking the diurnal temperature trends
665 over the year.

666
667 The nature of particulate nitrate can be estimated via fragmentation ratios of NO^+ and NO_2^+ ions detected by the ACSM
668 as described by (Farmer et al., 2010) for the AMS. A higher ratio (> 5) generally means a greater presence of organic
669 nitrates and a lower ratio (2–3) indicates inorganic ammonium nitrate. As the ACSM has a low mass resolving power, we
670 here estimate the ratio between m/Q 30 and m/Q 46 Th as a proxy for the $\text{NO}^+ : \text{NO}_2^+$ –ratio. We note that there is possible
671 interference of organic mass fragments at these m/Q –ratios. Nonetheless, we observe that the wintertime nitrate resembles
672 ammonium nitrate and the summertime nitrate hints towards the presence of organic nitrates (Figure 7g). This is in line
673 with the recent study stating that more than 50% of the nitrates detected in the sub-micron particles at SMEAR II are
674 estimated to contain organic nitrate functionalities (Äijälä et al., 2019). However, we should stress the fact that the data
675 coverage of wintertime was limited in the Äijälä et al. (2019) study that could lead to an overestimation of annual organic
676 nitrate mass fraction. Such high organic nitrate fraction could also explain some of the scatter observed in the ACSM NO_3
677 and MARGA NO_3 comparison discussed earlier in the manuscript (Figure A.3 and chapter 2.5 ACSM chemical speciation
678 validation). We observe no clear diurnal pattern in the fragmentation ratio.

679

680



681

682 **Figure 7** The median diurnal cycles of NR-PM₁ (panel a), Organic-to-inorganic ratio (panel b), organic aerosol (panel c), sulphate
 683 (panel d), nitrate (panel e), ammonium (panel f), $m/Q\ 30 : m/Q\ 46$ Th fragmentation ratio (panel g), and the ratio between measured
 684 and predicted ammonium (panel h). The y-axes represent the local time of day (UTC+2) and x-axes the month. The color scales
 685 present the mass concentration (panels a, c-f) or ratios (panels b, g-h). Note that the scaling of the color bar is different in all of the
 686 figures. Panels a-g include interpolation of the $14\ d \times 1\ h$ resolution data grid based on the MATLAB 2017a *contourf* function. Panel
 687 h has no interpolation involved due to the high noise level of the variable. The plot is produced with MATLAB 2017a *pcolor* function.

688

689 3.3 Wind direction dependence

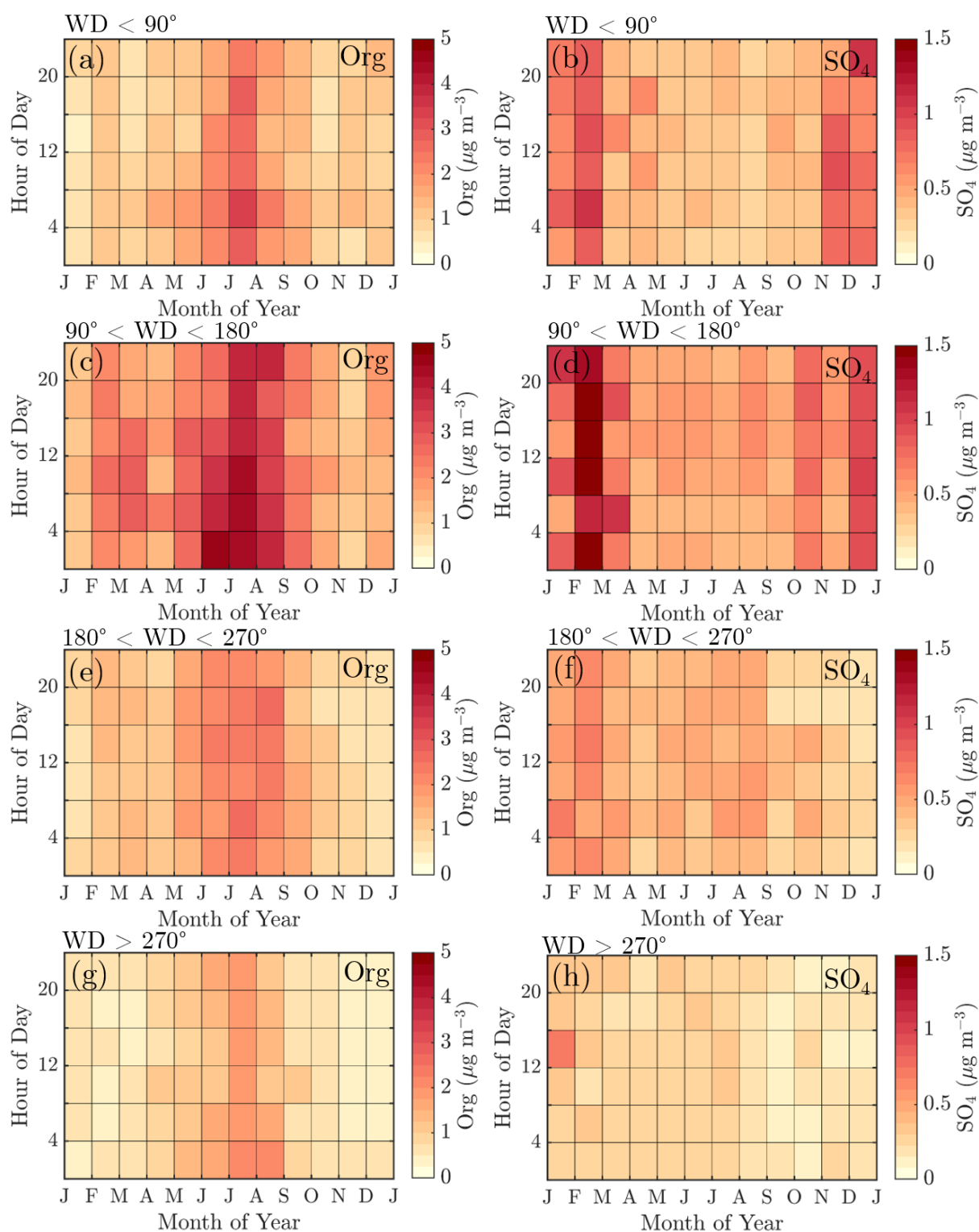
690 The wind direction plays a key role together with other meteorological conditions determining the aerosol chemical
691 composition at SMEAR II. While the sections above focus more on the role of radiation and temperature on sub-micron
692 aerosol composition, this section explains the role of wind direction and speed. We want to stress that this section does
693 not include any definite geographical source analysis of the NR-PM₁ components. A detailed trajectory analysis is a
694 better tool for understanding the actual footprint areas of air pollutants as wind direction analysis might lead to a
695 systematic bias in the pollutant origins due to prevailing weather patterns.

696 3.3.1 Wind sector dependent diurnal cycles of organics and sulphate

697 To explore the wind direction dependence of the seasonal cycles of the main NR-PM₁ chemical species, organics and
698 sulphate, we visualised their monthly median diurnal cycles with 4-hour time resolution (12 × 6 matrix) for four different
699 wind direction bins: 0–90° (I), 90–180° (II), 180–270° (III), and 270–360° (IV) in [Figure 8](#). The frequency of different
700 wind directions are depicted in [Figure A.1](#), showing that e.g. sector I was the least likely, while wind from sector III was
701 the dominant direction.

702
703 [The highest](#) organic aerosol loading [was](#) observed during summer for all of the wind direction bins (I – IV) with rather
704 modest diurnal variability, perhaps due to the coarse time resolution used ([Figure 8](#), left panels). The greatest organic
705 aerosol concentration was associated with sector II that covers the direction of the Korkeakoski sawmills located 6 – 7
706 km to the SW ([Figure 8c](#)). Moreover, the February peak in organic aerosol was also most distinguishable from sector II
707 ([Figure 8c](#)). Sulphate aerosol in turn was mostly detected with winds from sector I and II ([Figure 8](#), right panels). Sector
708 I shows a general wintertime enhancement ([Figure 8b](#)), whereas sector II shows a clear maximum during February ([Figure](#)
709 [8d](#)). The westerly sectors (III&IV) were associated with cleaner air ([Figures 8e–h](#)).

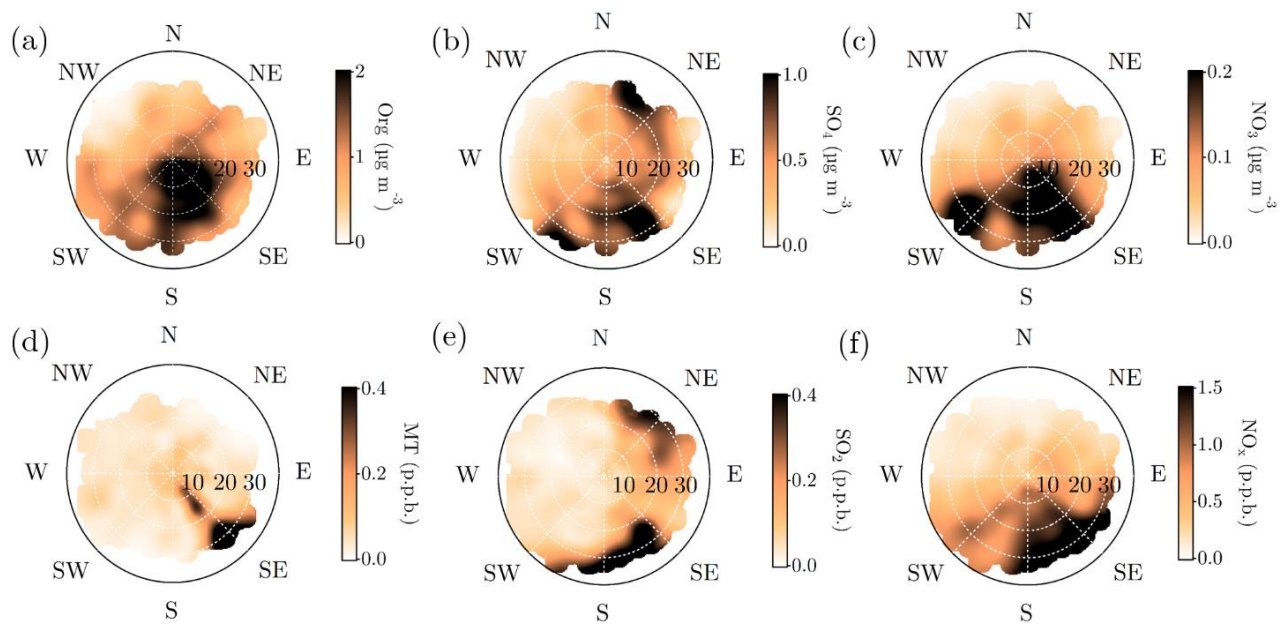
710



711

712 **Figure 8** Diurnal cycles of organic aerosol and sulphate divided into different wind direction bins: Panels a–b: wind direction $<90^\circ$,
 713 panels c–d: wind direction $90^\circ\text{--}180^\circ$, panels e–f: wind direction $180^\circ\text{--}270^\circ$, and panels g–h: wind direction $>270^\circ$. The y–axes represent
 714 the local time of day (UTC+2), and the x–axes the time of the year. The color scales represent the organic aerosol and sulphate aerosol
 715 mass concentrations in $\mu\text{g m}^{-3}$. [Figure A.1](#) introduces the likelihoods of each wind direction bin via a traditional wind rose plot.

716



718

719 **Figure 9** Openair polar plots for organic aerosol (panel a), sulphate (panel b), nitrate (panel c), monoterpenes (panel d), SO₂ (panel
 720 e), and NO_x (panel f). The distances from the origin indicates wind speeds in km h⁻¹. The wind speed grid lines are presented with
 721 white dashed circles. The colour scales represent the concentrations observed with each wind speed and direction combinations. As the
 722 figures do not indicate any likelihood of the wind speed and distance combinations, [Figure A.1](#) is important to keep in mind while
 723 interpreting them. Briefly, N–NE–E is the least probable wind direction, whereas S–SW–W is the most likely. Wind speeds generally
 724 stay below 20 km h⁻¹.

725

726 3.3.2 Openair: Organics and monoterpenes

727 Finally, we investigate the aerosol chemical composition dependence of wind speed and direction utilizing openair polar
 728 plots. As the polar plots do not take into account the frequency of certain wind direction and speed combinations, [Figures](#)
 729 [1c&d](#) and [Figure A.1](#) are important when drawing conclusions based on them.

730

731 Organic aerosol concentration at SMEAR II increased with S–SE winds as already visualised also in [Figure 8c](#) ([Figure](#)
 732 [9a](#)). The monoterpene mixing ratio also peaked, with a more narrow range of wind directions, analogous with the direction
 733 of the nearby Korkeakoski sawmills ([Figure 9d](#)). With higher wind speeds, monoterpenes were also observed from a
 734 wider span of wind directions. Organic aerosol showed wind speed dependence with S–SE winds with lower
 735 concentrations associated with wind speed exceeding 25 km h⁻¹ (ca. 6.9 m s⁻¹). A possible explanation is that the
 736 monoterpene emissions from the sawmills did not have time to oxidise and form SOA with such high wind speeds before
 737 reaching SMEAR II. Organic aerosol concentration was relatively constant outside the sawmill interference, though the
 738 lowest loadings were detected when air masses arrived with wind speeds exceeding 20 km h⁻¹ (ca. 5.5 m s⁻¹) from the
 739 NW sector. In contrast, monoterpene mixing ratio was rather constant with varying wind directions and wind speeds,
 740 obviously again apart from the sawmills direction (approximately 130°). Similar observations of the wind direction
 741 dependence of monoterpene mixing ratios have been reported before, with a subsequent organic aerosol mass
 742 concentration increase at SMEAR II with SW winds (Eerdekens et al., 2009; Liao et al., 2011).

743

744 A simplified seasonal analysis on aerosol chemical composition wind dependence was performed by investigating the
745 openair polar plots for all data recorded in February (**Figure A.1****Figure A.8**) and July (**Figure A.9**). Korkeakoski sawmills
746 represented the main monoterpene source in February as the concentration coinciding with air masses arriving from other
747 directions was negligible (**Figure A.8d**). In February, the sawmill emissions did not significantly enhance the organic
748 aerosol concentration at the site, due to low oxidation rates (monoterpene life time up to 10 h; Peräkylä et al., 2014) and
749 higher wind speeds (**Figure A.8a**). The organic aerosol concentration approached zero with NW winds during February
750 regardless of the wind speed. A major wind speed influence can be observed with SW winds, as higher wind speeds
751 coincide with elevated organic loading.

752

753 In July, the monoterpene mixing ratio increased regardless of the wind direction due to increased biogenic emissions from
754 the surrounding forest, but also the sawmill influence remained elevated (**Figure A.9d**). The monoterpene life time in July
755 is roughly two hours (Peräkylä et al., 2014) indicating an efficient photochemical sink. Thus, monoterpene sources are
756 likely not that far. The organic aerosol concentration was clearly overall elevated, however the overall easterly
757 interference was more pronounced compared to February (**Figures A.9a**). It could be linked to the high pressure systems
758 often associated with easterly winds that bring warm air and clear sky conditions to SMEAR II promoting BVOC
759 emissions and SOA formation as discussed earlier in the paper.

760

761 **3.3.3 Openair: Sulphate and SO₂**

762 Relatively high concentrations of sulphate aerosols and sulphur dioxide were detected with N–NE and SE–SW winds
763 (**Figures 9b&e**). Riuttanen et al. (2013) performed a HYSPLIT trajectory analysis for SMEAR II for 1996–2008 with SO₂
764 concentration fields showing similar results. They attribute the detected SO₂ to anthropogenic emission sources in St.
765 Petersburg, Baltic region, Kola Peninsula and the SE corner of the White Sea. **In addition to the major emission sources**
766 **introduced by Riuttanen et al. (2013), also paper and pulp industry are major known SO₂ emitters. Several paper and pulp**
767 **mills are situated in Finland, mostly NE and SE from SMEAR II (Metsäteollisuus, 2018). Another national major SO₂**
768 **source is certainly the Kilpilahti (Porvoo) oil refinery, located ~200 km S-SE from SMEAR II. This area represents the**
769 **most extensive oil refinery and chemical industry in the Nordic countries, and the SO₂ concentrations measured downwind**
770 **from the area have been close to those obtained from Kola Peninsula outflow (Sarnela et al., 2015).**

771

772 Large emission sources located SW of SMEAR II listed by EMEP (European Monitoring and Evaluation Programme)
773 did not stand out in the analysis performed by Riuttanen et al. (2013), but a wind direction dependence visible in the
774 current study, associated only with high wind speeds. Similar wind speed dependence was observed with SE–S and N–
775 NE winds as the concentration of sulphate and SO₂ clearly increased when wind speeds exceeded 20 km h⁻¹ (ca. 5.5 m s⁻¹).
776 Such wind speed dependence can be observed with long–range transported air pollutants: their transport is generally
777 more efficient with higher wind speeds. The results presented here are also consistent with hygroscopicity measurements
778 conducted at SMEAR II (Petäjä et al., 2005), where the hygroscopic growth factor was greatest when SO₂ rich air arrived
779 fast to the station from the NE.

780

781 NE and SE represent the major SO₂ sources in February. The NE SO₂ was detected with lower wind speed dependence
782 than generally observed (**Figures A.8b&e**). The lifetime of SO₂ is dependent on wet and dry deposition, and oxidation to
783 sulphate (photochemistry or aqueous phase chemistry in cloud droplets). These factors influence the likelihood of

784 detecting SO₂ from distant sources. The higher wintertime concentrations are also linked to the atmospheric boundary
785 layer dynamics, as discussed earlier. The SW and SE–S winds with wind speeds exceeding 16 km h⁻¹ (ca. 4.4 m s⁻¹) were
786 associated with sulphate during February (Figure A.8b). Sulphate was detected also with a wide range of wind directions
787 during low wind speeds. In the case of low wind speeds, it is hard to determine the wind direction accurately. However,
788 it was clear that sulphate was not associated with W–NW winds, as shown previously in the paper (Figure 8, right panels).

789
790 The sulphate openair polar plots for July (Figure A.9b) reveals that the sulphate transport was more wind speed dependent
791 than in February. Moreover, the wind directions linked to sulphate presence at SMEAR II were NW–N, NE, and E–SE,
792 but observed only when the wind speeds exceeded 16 km h⁻¹ (ca. 4.4 m s⁻¹). SO₂ was only observed with wind speeds
793 exceeded 16 km h⁻¹ (ca. 4.4 m s⁻¹) with NE winds (Figure A.9e). High wind speeds are needed in July to transport rather
794 short-lived pollutants, such as SO₂, to SMEAR II from distant sources.

795
796 As can be seen from Figures 9e, A.8e & A.9e, elevated SO₂ concentrations (dark areas in the concentration fields) are
797 associated with very specific, rather narrow ranges of easterly (mainly NE and SE) wind directions, and elevated wind
798 speeds (> 16–20 km h⁻¹). These figures illustrate the sensitivity of the recorded SO₂ concentration towards even moderate
799 wind direction and speed variations. As wind direction and speed can vary significantly in an inter-annual scale, also
800 inter-annual variability in SO₂ concentration can be expected. This could finally explain the SO₂ inter-annual variability
801 highlighted especially in winter months (Figure 4e). Such strong variability is not reflected further in the sulphate aerosol
802 (Figure 4b) year-to-year scales due to its long lifetime and build-up in the atmosphere.

803

804 3.3.4 Openair: Nitrate and NO_x

805 The nitrate concentration field visualised in Figure 9c was highest when wind blew from SE–SW. No wind speed
806 dependence could be attributed to the nitrate from E–SE, whereas for SW, nitrate concentration clearly elevated when
807 wind speed exceeded 20 km h⁻¹ (ca. 5.5 m s⁻¹). NO_x concentration, in turn, was not significantly elevated with SW winds
808 regardless of the wind speed, but shows similar behaviour to nitrate with SE–S winds (Figure 9f). The nitrates arriving
809 with SW likely spend more time in the atmosphere than in the case of SE–S source. A previous study focusing on organic
810 nitrates at SMEAR II linked their occurrence to SE winds (Kortelainen et al., 2017). They suggest night-time nitrate
811 radical oxidation of sawmill BVOCs as their major source. The same study attributes inorganic ammonium nitrate with
812 SW winds. The study was conducted in spring-time. Also our results suggested an increased organic nitrate presence in
813 spring compared to wintertime (Figure 7g).

814

815 In February, the nitrate concentration field resembles the overall concentration field depicted in Figure 9c, but highest
816 loadings were typically associated with low wind speeds from S–SE (Figure A.8c). The reason for not observing nitrate
817 with high wind speeds could be the fact that there is not enough time for nitrate aerosol formation. NO_x concentration
818 was overall elevated between NE and SE, and the clean SE–N sector had negligible NO_x loading (Figure A.8f). Despite
819 the NO_x availability in the North, no nitrate aerosol was observed. This could be due to limited ammonia availability in
820 winter time. Most NO_x was detected with E–SE winds when wind speed was 8–16 km h⁻¹ (ca. 2.2–4.4 m s⁻¹).

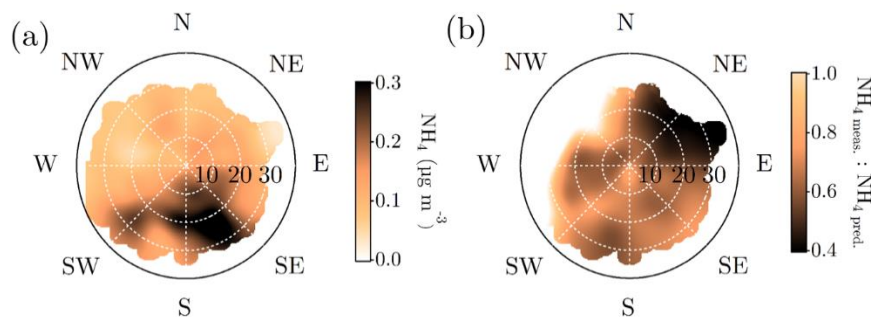
821

822 In July, SW winds blew most of the nitrate to SMEAR II (Figure A.9c). However, also slightly elevated concentrations
823 can be observed with S–SE winds (Figure A.9c). The nitrate associated with SW winds again requires high wind speeds.

824 The NO_x concentration was significantly lower in July compared to February, as already shown in Figure 4f (Figure A.9f).
825 No clear wind speed dependence was observed.

826

827 3.3.4 Openair: Ammonium and ion balance



828

829 **Figure 10** Openair polar plots for ammonium (panel a), and the ratio between measured and predicted ammonium (panel b). The
830 distances from the origin indicates wind speeds in km h^{-1} . The wind speed grid lines are presented with white dashed circles. The color
831 scales represent the concentration (panel a) and the unitless ammonium ion balance ratio (panel b) observed with each wind speed and
832 direction combinations. As the figures do not indicate any likelihood of the wind speed and distance combinations, Figure A.1 is
833 important to keep in mind while interpreting them. Briefly, N–NE–E is the least probable wind direction, whereas S–SW–W is the
834 most likely. Wind speeds generally stay below 20 km h^{-1} .

835

836 The overall polar plot for ammonium, visualised in Figure 10a, did not show elevated abundance with N-NE winds in
837 contrary to sulphate polar plot (Figure 9b). Moreover, the ammonium ion balance showed lowest values with N–NE winds
838 that often carry the sulphate-rich aerosols to SMEAR II (Figures 9b&10b). Such observations hint towards acidic
839 aerosols. Riva et al. (2019) observed acidic aerosols likely originating from the Kola Peninsula that support this
840 hypothesis. Moreover, the particle acidity further drove chemical transformations in the aerosol organic leading to a higher
841 presence of oligomers in the aerosol. Also the hygroscopicity analysis carried out at SMEAR II back in 2005 showed how
842 the particles arriving from NE were most hygroscopic (Petäjä et al., 2005) that is a property boosted in acidic aerosols.
843 The clean NW sector shows bright values for the ammonium balance field. Here, the ammonium balance exceeds one
844 due to the noisiness of the data introduced by both ammonium and nitrate used in the ammonium balance calculation
845 being below their detection limits during NW winds.

846 4 Conclusions

847 To better understand the boreal forest aerosol, an aerosol chemical speciation monitor (ACSM) was installed for long–
848 term monitoring of sub-micron aerosol chemical composition in 2012 at research site of SMEAR II. The measurements
849 continue to this day. Such measurements at the site had been previously conducted only in short-term intensive
850 measurement campaigns, leaving our understanding of the seasonal and year-to-year variability lacking. The current
851 study spans over the first seven years (2012–2018) of on-line monitoring of the sub-micron non-refractory aerosol
852 composition, finally providing this missing piece in SMEAR II aerosol documentation.

853

854 The median mass concentration over the measurement period was $2.3 \mu\text{g m}^{-3}$ (1.2 and $4.0 \mu\text{g m}^{-3}$ for the 25th and 75th
855 percentiles, respectively) of which 68% was organics, 20% sulphate, 6% nitrate, and 6% ammonium. Chloride
856 concentrations in the non-refractory sub-micron particles were negligible ($< 1\%$). As many factors, such as ambient

857 temperature, solar radiation, atmospheric boundary layer height and wind influence the aerosol particle concentrations
858 and trace gas emissions, oxidation and volatility, we observed a clear seasonal cycle in NR-PM₁ loading and composition.
859

860 During warm months, biogenic VOC emissions increase, and upon oxidation, produce SOA which represents a major
861 source of PM at SMEAR II. Organic aerosol mass concentration achieved its annual maximum in July (3.3, 1.7, and 4.6
862 $\mu\text{g m}^{-3}$ for median, 25th and 75th percentiles, respectively) that further lead to the annual maximum in the total NR-PM₁
863 loading (4.2, 2.2, and 5.7 $\mu\text{g m}^{-3}$ for median, 25th, 75th percentiles, respectively). Organics on average made up 80% of
864 the NR-PM₁ in summer. During the exceptionally hot Julys of 2014 and 2018, the organic aerosol concentrations were
865 up to 70% higher than the 7-year July mean. Most of the mass could be associated with increased biogenic SOA
866 production. The projected increase of heat wave frequency over Finland (and in general) will most likely influence the
867 loading and chemical composition of aerosol particles, and subsequently affect the Earth's radiative balance. Also from
868 this perspective, continuing the long-term measurements at SMEAR II is essential.
869

870 Winter months indicate low amounts of solar radiation and a shallow boundary layer. NO_x and SO₂, the main precursors
871 for particulate nitrate and sulphate, respectively, achieved their maximum mixing ratios during the darkest months while
872 emitted into the shallow boundary layer during the period of low photochemical activity. These species are generally
873 emitted in combustion processes that lead to high wintertime concentrations both due to the additional need of residential
874 heating as well as the shallow boundary layer prohibiting their vertical mixing. The maximum wintertime NR-PM₁
875 concentration was most commonly detected in February, and explained by an enhancement of inorganic aerosol species.
876 The particulate sulphate and nitrate peaked in February, which was later than their precursors, as a combined result of
877 wind patterns, deposition mechanisms and photochemistry affecting their formation and removal rates. The contribution
878 of inorganic aerosol species was ca. 50% of the total NR-PM₁ (2.7, 1.6, 5.1 $\mu\text{g m}^{-3}$ for median, 25th, 75th percentiles,
879 respectively) in February of which 30% was sulphate, 10% nitrate and 10% ammonium. Importantly, much of these
880 inorganic aerosol species were most likely from long-range transport. If emission regulations regarding SO₂ and NO_x
881 become stricter in the future in Europe, and especially in Russia, the wintertime NR-PM₁ might decrease significantly at
882 SMEAR II.
883

884 To our understanding, this is the longest time series reported describing the aerosol chemical composition measured on-
885 line in the boreal region. Long-term monitoring of changes introduced by emission regulations together with the changes
886 introduced by the changing climate, are crucial for understanding the aerosol-sensitivity of the (boreal) climate. Thus, we
887 keep the ACSM measurements on going at SMEAR II to obtain an even longer data set. The data presented here will be
888 publicly available, and we welcome collaborative work in utilising this information for broadening the understanding of
889 the boreal environment.

890 **Data availability**

891 The ACSM data are available at EBAS database (<http://ebas.nilu.no/>). The trace gas and meteorology data are available at the SMART
892 SMEAR data repository (<https://avaa.tdata.fi/web/smart>). Other data are available upon request from the corresponding authors.

893 **Author contributions**

894 LH, MÄ, ME, TP, MK, and DW designed the study. LH, MÄ and MA performed the ACSM measurements. LH processed and analysed
895 the ACSM data. JA and PR performed the PTR-MS measurements and data processing. HK provided and processed the Dekati impactor
896 data. PA performed the DMPS measurements and data processing. UM provided and processed the MARGA data. KL provided and
897 processed the Aethalometer data. DA performed satellite and trajectory analysis in [Figure A.6](#). LH performed the overall analysis, data
898 visualisation and wrote the paper. ME supervised the process. All authors commented and edited the paper.

899 **Competing interests**

900 The authors declare no conflict of interest.

901 **Acknowledgements**

902 First, we thank SMEAR II staff, Petri Keronen, Erkki Siivola and Frans Korhonen for measurement maintenance and support. We
903 thank the ACMCC, COST-COLOSSAL, and Aerodyne Research for the guidance towards high-quality instrument operation. We
904 thank Otso Peräkylä and Jenni Kontkanen for useful discussions. For financial support, we acknowledge the European Research
905 Council Starting Grant COALA. [We thank the anonymous reviewers for their expertise.](#)

907 **References**

- 908 Aalto, J., Porcar-Castell, A., Atherton, J., Kolari, P., Pohja, T., Hari, P., Nikinmaa, E., Petäjä, T., and Bäck, J.: Onset of
909 photosynthesis in spring speeds up monoterpene synthesis and leads to emission bursts, *Plant, cell and environment*, 38,
910 2299-2312, 2015.
- 911 Aalto, P., Hämeri, K., Becker, E., Weber, R., Salm, J., Mäkelä, J. M., Hoell, C., O’ Dowd, C. D., Hansson, H.-C., Väkevä,
912 M., Koponen, I., Gintautas, B., and Kulmala, M.: Physical characterization of aerosol particles during nucleation events,
913 *Tellus B: Chemical Physical Meteorology*, 53, 344-358, 2001.
- 914 Aas, W., Mortier, A., Bowersox, V., Cherian, R., Faluvegi, G., Fagerli, H., Hand, J., Klimont, Z., Galy-Lacaux, C.,
915 Lehmann, C. M., Lund Myhre, C., Myhre, G., Olivie, D., Sato, K., Quaas, J., Rao, P. S. P., Schultz, M., Shindell, D.,
916 Skeie, R. B., Stein, A., Takemura, T., Tsyro, S., Vet, R., and Xu, X.: Global and regional trends of atmospheric sulfur,
917 *Scientific reports*, 9, 953, 2019.
- 918 Aiken, A. C., Decarlo, P. F., Kroll, J. H., Worsnop, D. R., Huffman, J. A., Docherty, K. S., Ulbrich, I. M., Mohr, C.,
919 Kimmel, J. R., Sueper, D., Sun, Y., Zhang, Q., Trimborn, A., Northway, M., Ziemann, P. J., Canagaratna, M. R., Onasch,
920 T. B., Alfarra, R. M., Prevot, A. S. H., Dommen, J., Duplissy, J., Metzger, A., Baltensperger, U., and Jimenez, J. L.: O/C
921 and OM/OC ratios of primary, secondary, and ambient organic aerosols with high-resolution time-of-flight aerosol mass
922 spectrometry, *Environmental Science and Technology*, 42, 4478-4485, 2008.
- 923 Alfarra, M. R., Prevot, A. S., Szidat, S., Sandradewi, J., Weimer, S., Lanz, V. A., Schreiber, D., Mohr, M., and
924 Baltensperger, U.: Identification of the mass spectral signature of organic aerosols from wood burning emissions,
925 *Environmental Science and Technology*, 41, 5770-5777, 2007.
- 926 Allan, J. D., Delia, A. E., Coe, H., Bower, K. N., Alfarra, M. R., Jimenez, J. L., Middlebrook, A. M., Drewnick, F.,
927 Onasch, T. B., Canagaratna, M. R., Jayne, J. T., and Worsnop, D. R.: A generalised method for the extraction of
928 chemically resolved mass spectra from Aerodyne aerosol mass spectrometer data, *Journal of Aerosol Science*, 35, 909-
929 922, 2004.
- 930 Allan, J. D., Alfarra, M. R., Bower, K. N., Coe, H., Jayne, J. T., Worsnop, D. R., Aalto, P. P., Kulmala, M., Hyötyläinen,
931 T., Cavalli, F., and Laaksonen, A.: Size and composition measurements of background aerosol and new particle growth
932 in a Finnish forest during QUEST 2 using an Aerodyne Aerosol Mass Spectrometer, *Atmospheric Chemistry and Physics*,
933 6, 315-327, 2006.
- 934 Anttila, P., and Tuovinen, J.-P.: Trends of primary and secondary pollutant concentrations in Finland in 1994–2007,
935 *Atmospheric Environment*, 44, 30-41, 2010.
- 936 Barreira, F. M., Luis, Duporte, G., Parshintsev, J., Hartonen, K., Jussila, M., Aalto, J., Bäck, J., Kulmala, M., and
937 Riekkola, M.-L.: Emissions of biogenic volatile organic compounds from the boreal forest floor and understory, *Boreal
938 Environment Research*, 2017.
- 939 Barros, V., Field, C., Dokken, M., Mastrandrea, K., TE, M., M, B., KL, C., YO, E., RC, E., B, G., ES, G., ES, K., AN,
940 L., S, M., PR, M., and White, L.: IPCC, 2014: *Climaye Change 2014: Impacts, adaptation and vulnerability: Part B:*

941 Regional aspects. Contribution of Working Group II to the Fifth Assessment Report of the Intergovernmental Panel on
942 Climate Change, in: IPCC, 2014: Climate Change 2014: Impacts, adaptation and vulnerability: Part B: Regional aspects.
943 Contribution of Working Group II to the Fifth Assessment Report of the Intergovernmental Panel on Climate Change,
944 Cambridge University Press, 688, 2014.

945 Bauer, J. J., Yu, X. Y., Cary, R., Laulainen, N., and Berkowitz, C.: Characterization of the Sunset Semi-Continuous
946 Carbon Aerosol Analyzer, *Journal of the Air & Waste Management Association*, 59, 826-833, 10.3155/1047-
947 3289.59.7.826, 2009.

948 Bond, T. C., Streets, D. G., Yarber, K. F., Nelson, S. M., Woo, J. H., and Klimont, Z.: A technology-based global
949 inventory of black and organic carbon emissions from combustion, *Journal of Geophysical Research: Atmospheres*, 109,
950 2004.

951 Bond, T. C., and Bergstrom, R. W.: Light absorption by carbonaceous particles: An investigative review, *Aerosol Science
952 and Technology*, 40, 27-67, 2006.

953 Boucher, O., Randall, D., Artaxo, P., Bretherton, C., Feingold, G., Forster, P., Kerminen, V.-M., Kondo, Y., Liao, H., and
954 Lohmann, U.: Clouds and aerosols, in: *Climate change 2013: the physical science basis. Contribution of Working Group
955 I to the Fifth Assessment Report of the Intergovernmental Panel on Climate Change*, Cambridge University Press, 571-
956 657, 2013.

957 Canagaratna, M. R., Jayne, J. T., Jimenez, J. L., Allan, J. D., Alfarra, M. R., Zhang, Q., Onasch, T. B., Drewnick, F., Coe,
958 H., Middlebrook, A., Delia, A., Williams, L. R., Trimborn, A. M., Northway, M. J., DeCarlo, P. F., Kolb, C. E.,
959 Davidovits, P., and Worsnop, D. R.: Chemical and microphysical characterization of ambient aerosols with the aerodyne
960 aerosol mass spectrometer, *Mass Spectrometry Reviews*, 26, 185-222, 10.1002/mas.20115, 2007.

961 Carslaw, D. C., and Ropkins, K.: Openair—an R package for air quality data analysis, *Environmental Modelling &
962 Software*, 27, 52-61, 2012.

963 Cavalli, F., Facchini, M., Decesari, S., Emblico, L., Mircea, M., Jensen, N., and Fuzzi, S.: Size-segregated aerosol
964 chemical composition at a boreal site in southern Finland, during the QUEST project, *Atmospheric Chemistry and
965 Physics*, 6, 993-1002, 2006.

966 Cavalli, F., Viana, M., Yttri, K. E., Genberg, J., and Putaud, J.-P.: Toward a standardised thermal-optical protocol for
967 measuring atmospheric organic and elemental carbon: the EUSAAR protocol, *Atmospheric Measurement Techniques*, 3,
968 2010.

969 Collaud Coen, M., Andrews, E., Asmi, A., Baltensperger, U., Bukowiecki, N., Day, D., Fiebig, M., Fjæraa, A. M., Flentje,
970 H., Hyvärinen, A., Jefferson, A., Jennings, S. G., Kouvarakis, G., Lihavainen, H., Lund Myhre, C., Malm, W. C.,
971 Mihapopoulos, N., Molnar, J. V., O'Dowd, C., Ogren, J. A., Schichtel, B. A., Sheridan, P., Virkkula, A., Weingartner,
972 E., Weller, R., and Laj, P.: Aerosol decadal trends—Part 1: In-situ optical measurements at GAW and IMPROVE stations,
973 *Atmospheric Chemistry and Physics*, 13, 869-894, 2013.

974 Corrigan, A. L., Russell, L. M., Takahama, S., Äijälä, M., Ehn, M., Junninen, H., Rinne, J., Petäjä, T., Kulmala, M.,
975 Vogel, A. L., Hoffmann, T., Ebben, C. J., Geiger, F. M., Chhabra, P., Seinfeld, J. H., Worsnop, D. R., Song, W., Auld,
976 J., and Williams, J.: Biogenic and biomass burning organic aerosol in a boreal forest at Hyytiälä, Finland, during
977 HUMPPA-COPEC 2010, *Atmospheric Chemistry and Physics*, 13, 12233-12256, 10.5194/acp-13-12233-2013, 2013.

978 Crippa, M., Canonaco, F., Lanz, V., Äijälä, M., Allan, J., Carbone, S., Capes, G., Ceburnis, D., Dall'Osto, M., Day, D.,
979 DeCarlo, P. F., Ehn, M., Eriksson, A., Freney, E., Hildebrandt Ruiz, L., Hillamo, R., Jimenez, J. L., Junninen, H.,
980 Kiendler-Scharr, A., Kortelainen, A.-M., Kulmala, M., Laaksonen, A., Mensah, A. A., Mohr, C., Nemitz, E., O'Dowd,
981 C., Ovadnevaite, J., Pandis, S. N., Petäjä, T., Poulain, L., Saarikoski, S., Sellegri, K., Swietlicki, E., Tiitta, P., Worsnop,
982 D. R., Baltensperger, U., and Prévôt, A. S. H.: Organic aerosol components derived from 25 AMS data sets across Europe
983 using a consistent ME-2 based source apportionment approach, *Atmospheric Chemistry and Physics*, 14, 6159-6176,
984 2014.

985 Cubison, M., Ortega, A., Hayes, P., Farmer, D., Day, D., Lechner, M., Brune, W. H., Apel, E., Diskin, G., Fisher, J.,
986 Hecobian, A., Knapp, D., Mikoviny, T., Riemer, D., Satche, G., Sessions, W., Weber, R., Weinheimer, A., Wisthaler, A.,
987 and Jimenez, J. L.: Effects of aging on organic aerosol from open biomass burning smoke in aircraft and laboratory
988 studies, *Atmospheric Chemistry and Physics*, 11, 12049-12064, 2011.

989 Dada, L., Paasonen, P., Nieminen, T., Buenrostro Mazon, S., Kontkanen, J., Peräkylä, O., Lehtipalo, K., Hussein, T.,
990 Petäjä, T., Kerminen, V.-M., Bäck, J., and Kulmala, M.: Long-term analysis of clear-sky new particle formation events
991 and nonevents in Hyytiälä, *Atmospheric Chemistry and Physics*, 17, 6227-6241, 2017.

992 Daellenbach, K. R., Stefanelli, G., Bozzetti, C., Vlachou, A., Fermo, P., Gonzalez, R., Piazzalunga, A., Colombi, C.,
993 Canonaco, F., Hueglin, C., Kasper-Giebl, A., Jaffrezo, J.-L., Bianchi, F., Slowik, J. G., Baltensperger, U., El-Haddad, I.,
994 and Prévôt, A. S. H.: Long-term chemical analysis and organic aerosol source apportionment at nine sites in central
995 Europe: source identification and uncertainty assessment, *Atmospheric Chemistry and Physics*, 17, 13265-13282, 2017.

996 De Gouw, J., and Jimenez, J. L.: *Organic aerosols in the Earth's atmosphere*. ACS Publications, 2009.

997 DeCarlo, P., Ulbrich, I., Crouse, J., Foy, B. d., Dunlea, E., Aiken, A., Knapp, D., Weinheimer, A., Campos, T.,
998 Wennberg, P. J. A. C., and Physics: Investigation of the sources and processing of organic aerosol over the Central
999 Mexican Plateau from aircraft measurements during MILAGRO, 10, 5257-5280, 2010.

1000 Drinovec, L., Močnik, G., Zotter, P., Prévôt, A., Ruckstuhl, C., Coz, E., Rupakheti, M., Sciare, J., Müller, T.,
1001 Wiedensohler, A., and Hansen, A.: The " dual-spot" Aethalometer: an improved measurement of aerosol black carbon
1002 with real-time loading compensation, *Atmospheric Measurement Techniques*, 8, 1965-1979, 2015.

1003 Eerdekens, G., Yassaa, N., Sinha, V., Aalto, P., Aufmhoff, H., Arnold, F., Fiedler, V., Kulmala, M., and Williams, J.:
1004 VOC measurements within a boreal forest during spring 2005: on the occurrence of elevated monoterpene concentrations
1005 during night time intense particle concentration events, *Atmospheric Chemistry and Physics*, 9, 8331-8350, 2009.

1006 Fanourgakis, G. S., Kanakidou, M., Nenes, A., Bauer, S. E., Bergman, T., Carslaw, K. S., Grini, A., Hamilton, D. S.,
1007 Johnson, J. S., Karydis, V. A., Kirkevåg, A., Kodros, J. K., Lohmann, U., Luo, G., Makkonen, R., Matsui, H., Neubauer,
1008 D., Pierce, J. R., Schmale, J., Stier, P., Tsigaridis, K., van Noije, T., Wang, H., Watson-Parris, D., Westervelt, D. M.,
1009 Yang, Y., Yoshioka, M., Daskalakis, N., Decesari, S., Gysel-Beer, M., Kalivitis, N., Liu, X., Mahowald, N. M.,
1010 Myriokefalitakis, S., Schrödner, R., Sfakianaki, M., Tsimpidi, A. P., Wu, M., and Yu, F.: Evaluation of global simulations
1011 of aerosol particle and cloud condensation nuclei number, with implications for cloud droplet formation, *Atmospheric
1012 Chemistry and Physics*, 19, 8591-8617, 2019.

1013 Farmer, D., Matsunaga, A., Docherty, K., Surratt, J., Seinfeld, J., Ziemann, P., and Jimenez, J.: Response of an aerosol
1014 mass spectrometer to organonitrates and organosulfates and implications for atmospheric chemistry, *Proceedings of the
1015 National Academy of Sciences*, 107, 6670-6675, 2010.

1016 Finessi, E., Decesari, S., Paglione, M., Giulianelli, L., Carbone, C., Gilardoni, S., Fuzzi, S., Saarikoski, S., Raatikainen,
1017 T., Hillamo, R., Allan, J. D., Mentel, T. F., Tiitta, P., Laaksonen, A., Petäjä, T., Kulmala, M., Worsnop, D., and Facchini,
1018 M.: Determination of the biogenic secondary organic aerosol fraction in the boreal forest by NMR spectroscopy,
1019 *Atmospheric Chemistry and Physics*, 12, 941-959, 2012.

1020 An exceptionally long heatwave: https://en.ilmatieteenlaitos.fi/press-release-archive/-/journal_content/56/31422/10014539,
1021 access: 13 January 2020, 2014.

1022 Gauthier, S., Bernier, P., Kuuluvainen, T., Shvidenko, A., and Schepaschenko, D.: Boreal forest health and global change,
1023 *Science*, 349, 819-822, 2015.

1024 Grieshop, A., Donahue, N., and Robinson, A.: Laboratory investigation of photochemical oxidation of organic aerosol
1025 from wood fires 2: analysis of aerosol mass spectrometer data, *Atmospheric Chemistry and Physics*, 9, 2227-2240, 2009.

1026 Guenther, A. B., Zimmerman, P. R., Harley, P. C., Monson, R. K., and Fall, R.: Isoprene and monoterpene emission rate
1027 variability: model evaluations and sensitivity analyses, *Journal of Geophysical Research: Atmospheres*, 98, 12609-12617,
1028 1993.

1029 Hakola, H., Hellén, H., Hemmilä, M., Rinne, J., and Kulmala, M.: In situ measurements of volatile organic compounds
1030 in a boreal forest, *Atmospheric Chemistry and Physics*, 12, 11665-11678, 2012.

1031 Hari, P., and Kulmala, M.: Station for measuring ecosystem-atmosphere relations (SMEAR II), *Boreal Environment
1032 Research*, 10, 315-322, 2005.

1033 Heald, C., Henze, D., Horowitz, L., Feddema, J., Lamarque, J. F., Guenther, A., Hess, P., Vitt, F., Seinfeld, J., Goldstein,
1034 A., and Fung, I.: Predicted change in global secondary organic aerosol concentrations in response to future climate,
1035 emissions, and land use change, *Journal of Geophysical Research: Atmospheres*, 113, 2008.

1036 Hong, J., Häkkinen, S. A., Paramonov, M., Äijälä, M., Hakala, J., Nieminen, T., Mikkilä, J., Prisle, N. L., Kulmala, M.,
1037 Riipinen, I., Bilde, M., Kerminen, V.-M., and Petäjä, T.: Hygroscopicity, CCN and volatility properties of submicron
1038 atmospheric aerosol in a boreal forest environment during the summer of 2010, *Atmospheric Chemistry and Physics*, 14,
1039 4733-4748, 2014.

1040 Hong, J., Äijälä, M., Häme, S. A., Hao, L., Duplissy, J., Heikkinen, L. M., Nie, W., Mikkilä, J., Kulmala, M., Prisle, N.
1041 L., Virtanen, A., Ehn, M., Paasonen, P., Worsnop, D. R., Riipinen, I., Petäjä, T., and Kerminen, V.-M.: Estimates of the
1042 organic aerosol volatility in a boreal forest using two independent methods, *Atmospheric Chemistry and Physics*, 17,
1043 4387-4399, 2017.

1044 Häkkinen, S., Äijälä, M., Lehtipalo, K., Junninen, H., Backman, J., Virkkula, A., Nieminen, T., Vestenius, M., Hakola,
1045 H., Ehn, M., Worsnop, D., Kulmala, M., Petäjä, T., and Riipinen, I.: Long-term volatility measurements of submicron
1046 atmospheric aerosol in Hyytiälä, Finland, *Atmospheric Chemistry and Physics*, 12, 10771-10786, 2012.

1047 Jimenez, J. L., Canagaratna, M. R., Donahue, N. M., Prevot, A. S. H., Zhang, Q., Kroll, J. H., DeCarlo, P. F., Allan, J.
1048 D., Coe, H., Ng, N. L., Aiken, A. C., Docherty, K. S., Ulbrich, I. M., Grieshop, A. P., Robinson, A. L., Duplissy, J., Smith,
1049 J. D., Wilson, K. R., Lanz, V. A., Hueglin, C., Sun, Y. L., Tian, J., Laaksonen, A., Raatikainen, T., Rautiainen, J.,
1050 Vaattovaara, P., Ehn, M., Kulmala, M., Tomlinson, J. M., Collins, D. R., Cubison, M. J., Dunlea, E. J., Huffman, J. A.,
1051 Onasch, T. B., Alfarra, M. R., Williams, P. I., Bower, K., Kondo, Y., Schneider, J., Drewnick, F., Borrmann, S., Weimer,
1052 S., Demerjian, K., Salcedo, D., Cottrell, L., Griffin, R., Takami, A., Miyoshi, T., Hatakeyama, S., Shimono, A., Sun, J.
1053 Y., Zhang, Y. M., Dzepina, K., Kimmel, J. R., Sueper, D., Jayne, J. T., Herndon, S. C., Trimborn, A. M., Williams, L. R.,
1054 Wood, E. C., Middlebrook, A. M., Kolb, C. E., Baltensperger, U., and Worsnop, D. R.: Evolution of Organic Aerosols in
1055 the Atmosphere, *Science*, 326, 1525-1529, 10.1126/science.1180353, 2009.

1056 Junninen, H., Lauri, A., Keronen, P., Aalto, P., Hiltunen, V., Hari, P., and Kulmala, M.: Smart-SMEAR: on-line data
1057 exploration and visualization tool for SMEAR stations, *Boreal Environment Research*, 2009.

1058 Kim, S., Sinclair, V. A., Räisänen, J., and Ruuhela, R.: Heat waves in Finland: Present and projected summertime extreme
1059 temperatures and their associated circulation patterns, *International Journal of Climatology*, 38, 1393-1408, 2018.

1060 Kontkanen, J., Paasonen, P., Aalto, J., Bäck, J., Rantala, P., Petäjä, T., and Kulmala, M.: Simple proxies for estimating
1061 the concentrations of monoterpenes and their oxidation products at a boreal forest site, *Atmospheric Chemistry and*
1062 *Physics*, 16, 13291-13307, 2016.

1063 Kortelainen, A., Hao, L., Tiitta, P., Jaatinen, A., Miettinen, P., Kulmala, M., Smith, J. N., Laaksonen, A., Worsnop, D.
1064 R., and Virtanen, A.: Sources of particulate organic nitrates in the boreal forest in Finland, *Boreal Environment Research*,
1065 22, 13-26, 2017.

1066 Kourtchev, I., Ruuskanen, T., Maenhaut, W., Kulmala, M., and Claeys, M.: Observation of 2-methyltetrols and related
1067 photo-oxidation products of isoprene in boreal forest aerosols from Hyytiälä, Finland, *Atmospheric Chemistry and*
1068 *Physics*, 5, 2761-2770, 2005.

1069 Kourtchev, I., Fuller, S., Aalto, J., Ruuskanen, T. M., McLeod, M. W., Maenhaut, W., Jones, R., Kulmala, M., and
1070 Kalberer, M.: Molecular composition of boreal forest aerosol from Hyytiälä, Finland, using ultrahigh resolution mass
1071 spectrometry, *Environmental Science and Technology*, 47, 4069-4079, 2013.

1072 Kulmala, M., Pirjola, L., and Mäkelä, J. M.: Stable sulphate clusters as a source of new atmospheric particles, *Nature*,
1073 404, 66, 2000.

1074 Kulmala, M., Vehkamäki, H., Petäjä, T., Dal Maso, M., Lauri, A., Kerminen, V.-M., Birmili, W., and McMurry, P.:
1075 Formation and growth rates of ultrafine atmospheric particles: a review of observations, *Journal of Aerosol Science*, 35,
1076 143-176, 2004.

1077 Kulmala, M.: Build a global Earth observatory, *Nature*, 553, 21-23, 10.1038/d41586-017-08967-y, 2018.

1078 Liao, L., Dal Maso, M., Taipale, R., Rinne, J., Ehn, M., Junninen, H., Äijälä, M., Nieminen, T., Alekseychik, P.,
1079 Hulkkonen, M., Worsnop, D., Kerminen, V.-M., and Kulmala, M.: Monoterpene pollution episodes in a forest
1080 environment: indication of anthropogenic origin and association with aerosol particles, *Boreal Environment Research*,
1081 16, 288-303, 2011.

1082 Lim, H.-J., and Turpin, B.: Origins of primary and secondary organic aerosol in Atlanta: Results of time-resolved
1083 measurements during the Atlanta supersite experiment, *Environmental Science and Technology*, 36, 4489-4496, 2002.

1084 Lindinger, W., and Jordan, A.: Proton-transfer-reaction mass spectrometry (PTR-MS): on-line monitoring of volatile
1085 organic compounds at pptv levels, *Chemical Society Reviews*, 27, 347-375, 1998.

1086 Liu, P. S., Deng, R., Smith, K. A., Williams, L. R., Jayne, J. T., Canagaratna, M. R., Moore, K., Onasch, T. B., Worsnop,
1087 D. R., and Deshler, T.: Transmission efficiency of an aerodynamic focusing lens system: Comparison of model
1088 calculations and laboratory measurements for the Aerodyne Aerosol Mass Spectrometer, *Aerosol Science and*
1089 *Technology*, 41, 721-733, 2007.

1090 Makkonen, U., Virkkula, A., Mäntykenttä, J., Hakola, H., Keronen, P., Vakkari, V., and Aalto, P. P.: Semi-continuous
1091 gas and inorganic aerosol measurements at a Finnish urban site: comparisons with filters, nitrogen in aerosol and gas
1092 phases, and aerosol acidity, *Atmospheric Chemistry and Physics*, 12, 5617-5631, 2012.

1093 Makkonen, U., Virkkula, A., Hellén, H., Hemmilä, M., Sund, J., Äijälä, M., Ehn, M., Junninen, H., Keronen, P., Petäjä,
1094 T., Worsnop, D., Kulmala, M., and Hakola, H.: Semi-continuous gas and inorganic aerosol measurements at a boreal
1095 forest site: seasonal and diurnal cycles of NH₃, HONO and HNO₃, *Boreal Environment Research*, 19 (supp. B), 311-328,
1096 2014.

1097 McGrath-Spangler, E. L., and Denning, A. S.: Global seasonal variations of midday planetary boundary layer depth from
1098 CALIPSO space-borne LIDAR, *Journal of Geophysical Research: Atmospheres*, 118, 1226-1233, 2013.

1099 Pulp and Paper Industry: Paper-, paperboard and pulpmills in Finland: [https://www.forestindustries.fi/statistics/pulp-and-](https://www.forestindustries.fi/statistics/pulp-and-paper-industry/)
1100 [paper-industry/](https://www.forestindustries.fi/statistics/pulp-and-paper-industry/), access: January 15 2020, 2018.

1101 Middlebrook, A. M., Bahreini, R., Jimenez, J. L., and Canagaratna, M. R.: Evaluation of composition-dependent
1102 collection efficiencies for the aerodyne aerosol mass spectrometer using field data, *Aerosol Science and Technology*, 46,
1103 258-271, 2012.

1104 Mikhailov, E. F., Mironova, S., Mironov, G., Vlasenko, S., Panov, A., Chi, X., Walter, D., Carbone, S., Artaxo, P.,
1105 Heimann, M., Lavric, J., Pöschl, U., and Andreae, M.: Long-term measurements (2010–2014) of carbonaceous aerosol
1106 and carbon monoxide at the Zotino Tall Tower Observatory (ZOTTO) in central Siberia, *Atmospheric Chemistry and*
1107 *Physics*, 17, 14365-14392, 2017.

1108 Myhre, G., Samset, B. H., Schulz, M., Balkanski, Y., Bauer, S., Berntsen, T. K., Bian, H., Bellouin, N., Chin, M., and
1109 Diehl, T.: Radiative forcing of the direct aerosol effect from AeroCom Phase II simulations, *Atmospheric Chemistry and*
1110 *Physics*, 13, 1853, 2013.

1111 Ng, N. L., Herndon, S. C., Trimborn, A., Canagaratna, M. R., Croteau, P. L., Onasch, T. B., Sueper, D., Worsnop, D. R.,
1112 Zhang, Q., Sun, Y. L., and Jayne, J. T.: An Aerosol Chemical Speciation Monitor (ACSM) for Routine Monitoring of the
1113 Composition and Mass Concentrations of Ambient Aerosol, *Aerosol Science and Technology*, 45, 780-794, 2011.

1114 Paasonen, P., Asmi, A., Petäjä, T., Kajos, M. K., Äijälä, M., Junninen, H., Holst, T., Abbatt, J. P., Arneth, A., Denier van
1115 der Gon, H., Hamed, A., Hoffer, A., Laakso, L., Laaksonen, A., Leitch, W. R., Plass-Dülmer, C., Pryor, S. C., Räsänen,
1116 P., Swietlicki, E., Wiedensohler, A., Worsnop, D. R., Kerminen, V.-M., and Kulmala, M.: Warming-induced increase in
1117 aerosol number concentration likely to moderate climate change, *Nature Geoscience*, 6, 438, 2013.

1118 Pachauri, R. K., and Meyer, L.: Climate change 2014: Synthesis Report-Summary for Policymakers, Intergovernmental
1119 Panel on Climate Change (IPCC), Climate change 2014: Synthesis Report-Summary for Policymakers, 2014.

1120 Patokoski, J., Ruuskanen, T. M., Kajos, M. K., Taipale, R., Rantala, P., Aalto, J., Ryyppö, T., Nieminen, T., Hakola, H.,
1121 and Rinne, J.: Sources of long-lived atmospheric VOCs at the rural boreal forest site, SMEAR II, *Atmospheric Chemistry*
1122 *and Physics*, 15, 13413-13432, 2015.

1123 Peräkylä, O., Vogt, M., Tikkanen, O.-P., Laurila, T., Kajos, M. K., Rantala, P. A., Patokoski, J., Aalto, J., Yli-Juuti, T.,
1124 Ehn, M., Sipilä, M., Paasonen, P., Rissanen, M., Nieminen, T., Taipale, R., Keronen, P., Lappalainen, H. K., Ruuskanen,
1125 T. M., Rinne, J., Kerminen, V.-M., Kulmala, M., Bäck, J., and Petäjä, T.: Monoterpenes' oxidation capacity and rate over
1126 a boreal forest, *Boreal Environment Research*, 19, 293-310, 2014.

1127 Petit, J.-E., Favez, O., Albinet, A., and Canonaco, F.: A user-friendly tool for comprehensive evaluation of the
1128 geographical origins of atmospheric pollution: Wind and trajectory analyses, *Environmental modelling and software*, 88,
1129 183-187, 2017.

1130 Petäjä, T., Kerminen, V.-M., Hämeri, K., Vaattovaara, P., Joutsensaari, J., Junkermann, W., Laaksonen, A., and Kulmala,
1131 M.: Effects of SO₂ oxidation on ambient aerosol growth in water and ethanol vapours, *Atmospheric Chemistry and*
1132 *Physics*, 5, 767-779, 2005.

1133 Pirinen, P., Simola, H., Aalto, J., Kaukoranta, J.-P., Karlsson, P., and Ruuhela, R.: Tilastoja suomen ilmastosta 1981-
1134 2010, Ilmatieteen laitos, 2012.

1135 Prävälje, R.: Major perturbations in the Earth's forest ecosystems. Possible implications for global warming, *Earth-*
1136 *Science Reviews*, 185, 544-571, 2018.

1137 Ramanathan, V., Crutzen, P., Kiehl, J., and Rosenfeld, D.: Aerosols, climate, and the hydrological cycle, *Science*, 294,
1138 2119-2124, 2001.

1139 Rantala, P., Aalto, J., Taipale, R., Ruuskanen, T., and Rinne, J.: Annual cycle of volatile organic compound exchange
1140 between a boreal pine forest and the atmosphere, *Biogeosciences*, 2015.

1141 Ridley, D., Heald, C., Ridley, K., and Kroll, J.: Causes and consequences of decreasing atmospheric organic aerosol in
1142 the United States, *Proceedings of the National Academy of Sciences*, 115, 290-295, 2018.

1143 Riuttanen, L., Hulkkonen, M., Maso, M. D., Junninen, H., and Kulmala, M.: Trajectory analysis of atmospheric transport
1144 of fine particles, SO₂, NO_x and O₃ to the SMEAR II station in Finland in 1996–2008, *Atmospheric Chemistry and*
1145 *Physics*, 13, 2153-2164, 2013.

1146 Riva, M., Heikkinen, L., Bell, D., Peräkylä, O., Zha, Q., Schallhart, S., Rissanen, M., Imre, D., Petäjä, T., Thornton, J.,
1147 Zelenyuk, A., and Ehn, M.: Chemical transformations in monoterpene-derived organic aerosol enhanced by inorganic
1148 composition, *npj Climate and Atmospheric Science*, 2, 2, 2019.

1149 Russell, L. M.: Aerosol organic-mass-to-organic-carbon ratio measurements, *Environmental Science and Technology*,
1150 37, 2982-2987, 2003.

1151 Saarikoski, S., Mäkelä, T., Hillamo, R., Aalto, P. P., Kerminen, V.-M., and Kulmala, M.: Physico-chemical
1152 characterization and mass closure of size-segregated atmospheric aerosols in Hyytiälä, Finland, *Boreal Environment*
1153 *Research*, 10, 385-400, 2005.

1154 Sarnela, N., Jokinen, T., Nieminen, T., Lehtipalo, K., Junninen, H., Kangasluoma, J., Hakala, J., Taipale, R.,
1155 Schobesberger, S., Sipilä, M., Larnimaa, K., Westerholm, H., Heijari, J., Kerminen, V.-M., Petäjä, T., and Kulmala, M.:
1156 Sulphuric acid and aerosol particle production in the vicinity of an oil refinery, *Atmospheric Environment*, 119, 156-166,
1157 2015.

1158 Schmidt, A., Leadbetter, S., Theys, N., Carboni, E., Witham, C. S., Stevenson, J. A., Birch, C. E., Thordarson, T.,
1159 Turnock, S., Barsotti, S., Delaney, L., Feng, W., Grainger, R. G., Hort, M. C., Höskuldsson, Á., Ialongo, I., Ilyinskaya,
1160 E., Jóhannsson, T., Kenny, P., Mather, T. A., Richards, N. A. D., and Shepherd, J.: Satellite detection, long-range
1161 transport, and air quality impacts of volcanic sulfur dioxide from the 2014–2015 flood lava eruption at Bárðarbunga
1162 (Iceland), *Journal of Geophysical Research: Atmospheres*, 120, 9739-9757, 2015.

1163 Schneider, J., Weimer, S., Drewnick, F., Borrmann, S., Helas, G., Gwaze, P., Schmid, O., Andreae, M., and Kirchner, U.:
1164 Mass spectrometric analysis and aerodynamic properties of various types of combustion-related aerosol particles,
1165 *International Journal of Mass Spectrometry*, 258, 37-49, 2006.

1166 Settele, J., Scholes, R., Betts, R. A., Bunn, S., Leadley, P., Nepstad, D., Overpeck, J., Taboada, M. A., Fischlin, A., and
1167 Moreno, J. M.: Terrestrial and inland water systems, in: *Climate Change 2014 Impacts, Adaptation and Vulnerability:*
1168 *Part A: Global and Sectoral Aspects*, Cambridge University Press, 271-360, 2014.

1169 Simon, H., Reff, A., Wells, B., Xing, J., and Frank, N.: Ozone trends across the United States over a period of decreasing
1170 NO_x and VOC emissions, *Environmental Science and Technology*, 49, 186-195, 2014.

1171 Sinclair, V. A., Mikkola, J., Rantanen, M., and Räisänen, J.: The summer 2018 heatwave in Finland, *Weather*, 2019.

1172 Spracklen, D. V., Mickley, L. J., Logan, J. A., Hudman, R. C., Yevich, R., Flannigan, M. D., and Westerling, A. L.:
1173 Impacts of climate change from 2000 to 2050 on wildfire activity and carbonaceous aerosol concentrations in the western
1174 United States, *Journal of Geophysical Research: Atmospheres*, 114, 2009.

1175 Stefenelli, G., Pospisilova, V., Lopez-Hilfiker, F. D., Daellenbach, K. R., Hüglin, C., Tong, Y., Baltensperger, U., Prevot,
1176 A. S. H., and Slowik, J. G.: Organic aerosol source apportionment in Zurich using an extractive electrospray ionization
1177 time-of-flight mass spectrometer (EESI-TOF-MS) – Part 1: Biogenic influences and day–night chemistry in summer,
1178 *Atmospheric Chemistry and Physics*, 2019, 14825-14848, 2019.

1179 Taipale, R., Ruuskanen, T., Rinne, J., Kajos, M., Hakola, H., Pohja, T., and Kulmala, M.: Technical Note: Quantitative
1180 long-term measurements of VOC concentrations by PTR-MS – measurement, calibration, and volume mixing ratio
1181 calculation methods, *Atmospheric Chemistry and Physics*, 8, 6681-6698, <https://doi.org/10.5194/acp-8-6681-2008>, 2008.

1182 Tsigaridis, K., Krol, M., Dentener, F., Balkanski, Y., Lathiere, J., Metzger, S., Hauglustaine, D., and Kanakidou, M.:
1183 Change in global aerosol composition since preindustrial times, *Atmospheric Chemistry and Physics*, 6, 5143-5162, 2006.

1184 Tunved, P., Hansson, H.-C., Kerminen, V.-M., Ström, J., Dal Maso, M., Lihavainen, H., Viisanen, Y., Aalto, P.,
1185 Komppula, M., and Kulmala, M.: High natural aerosol loading over boreal forests, *Science*, 312, 261-263, 2006.

1186 Tuononen, M., O'Connor, E. J., and Sinclair, V. A.: Evaluating solar radiation forecast uncertainty, *Atmospheric
1187 Chemistry and Physics*, 19, 1985-2000, 2019.

1188 Turpin, B. J., and Lim, H.-J.: Species contributions to PM_{2.5} mass concentrations: Revisiting common assumptions for
1189 estimating organic mass, *Aerosol Science and Technology*, 35, 602-610, 2001.

1190 Wang, K., Dickinson, R. E., Su, L., and Trenberth, K.: Contrasting trends of mass and optical properties of aerosols over
1191 the Northern Hemisphere from 1992 to 2011, *Atmospheric Chemistry and Physics*, 12, 9387-9398, 2012.

1192 Williams, J., Crowley, J., Fischer, H., Harder, H., Martinez, M., Petaja, T., Rinne, J., Back, J., Boy, M., Hakala, J., Kajos,
1193 M., Keronen, P., Rantala, P., Aalto, J., Aaltonen, H., Paatero, J., Vesala, T., Hakola, H., Levula, J., Pohja, T., Herrmann,
1194 F., Auld, J., Mesarchaki, E., Song, W., Yassaa, N., Nolscher, A. C., Johnson, A. M., Custer, T., Sinha, V., Thieser, J.,
1195 Povesle, N., Taraborrelli, D., Tang, M. J., Bozem, H., Hosaynali-Beygi, Z., Axinte, R., Oswald, R., Novelli, A., Kubistin,
1196 D., Hens, K., Javed, U., Trawny, K., Breitenberger, C., Hidalgo, P. J., Ebben, C. J., Geiger, F. M., Corrigan, A. L., Russell,
1197 L. M., Ouwersloot, H. G., Vila-Guerau De Arellano, J., Ganzeveld, L., Vogel, A., Beck, M., Bayerle, A., Kampf, C. J.,
1198 Bertelmann, M., Kollner, F., Hoffmann, T., Valverde, J., Gonzalez, D., Riekkola, M.-L., Kulmala, M., and Lelieveld, J.:
1199 The summertime Boreal forest field measurement intensive (HUMPPA-COPEC-2010): an overview of meteorological
1200 and chemical influences, *Atmospheric Chemistry and Physics*, 2011.

1201 Vlachou, A., Daellenbach, K. R., Bozzetti, C., Chazeau, B., Salazar, G. A., Szidat, S., Jaffrezo, J.-L., Hueglin, C.,
1202 Baltensperger, U., Haddad, I. E., and Prévôt, A. S. H.: Advanced source apportionment of carbonaceous aerosols by
1203 coupling offline AMS and radiocarbon size-segregated measurements over a nearly 2-year period, *Atmospheric
1204 Chemistry and Physics*, 18, 6187-6206, 2018.

1205 Zhang, Q., Jimenez, J. L., Canagaratna, M., Allan, J., Coe, H., Ulbrich, I., Alfarra, M., Takami, A., Middlebrook, A., Sun,
1206 Y., Dzepina, K., Dunlea, E. J., Docherty, K. S., DeCarlo, P. F., Salcedo, D., Onasch, T., Borrmann, S., Weimer, S.,
1207 Demerjian, K., Williams, P., Bower, K., Bahreini, R., Cottrell, L., Griffin, R., Rautiainen, J., Sun, J. Y., Zhang, Y. M.,
1208 and Worsnop, D.: Ubiquity and dominance of oxygenated species in organic aerosols in anthropogenically-influenced
1209 Northern Hemisphere midlatitudes, *Geophysical Research Letters*, 34, 2007a.

1210 Zhang, Q., Jimenez, J. L., Worsnop, D. R., and Canagaratna, M.: A case study of urban particle acidity and its influence
1211 on secondary organic aerosol, *Environmental Science and Technology*, 41, 3213-3219, 2007b.

1212 Zhang, Y., Favez, O., Canonaco, F., Liu, D., Močnik, G., Amodeo, T., Sciare, J., Prévôt, A. S., Gros, V., and Albinet, A.:
1213 Evidence of major secondary organic aerosol contribution to lensing effect black carbon absorption enhancement, *npj
1214 Climate and Atmospheric Science*, 1, 47, 2018.

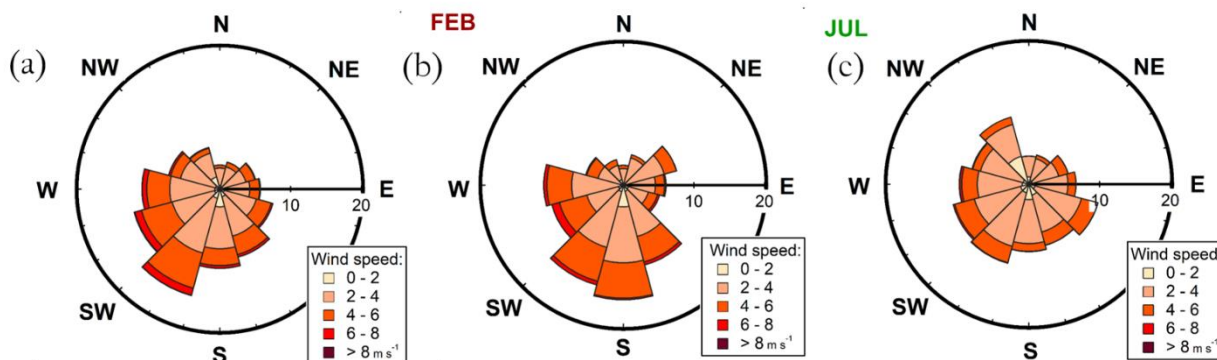
1215 Zhao, D., Buchholz, A., Tillmann, R., Kleist, E., Wu, C., Rubach, F., Kiendler-Scharr, A., Rudich, Y., Wildt, J., and
1216 Mentel, T. F.: Environmental conditions regulate the impact of plants on cloud formation, *Nature Communications*, 8,
1217 14067, 2017.

1218 Äijälä, M., Heikkinen, L., Fröhlich, R., Canonaco, F., Prévôt, A. S., Junninen, H., Petäjä, T., Kulmala, M., Worsnop, D.,
1219 and Ehn, M.: Resolving anthropogenic aerosol pollution types—deconvolution and exploratory classification of pollution
1220 events, *Atmospheric Chemistry and Physics*, 17, 3165-3197, 2017.

1221 Äijälä, M., Daellenbach, K. R., Canonaco, F., Heikkinen, L., Junninen, H., Petäjä, T., Kulmala, M., Prévôt, A. S., and
1222 Ehn, M.: Constructing a data-driven receptor model for organic and inorganic aerosol—a synthesis analysis of eight mass
1223 spectrometric data sets from a boreal forest site, *Atmospheric Chemistry and Physics*, 19, 3645-3672, 2019.

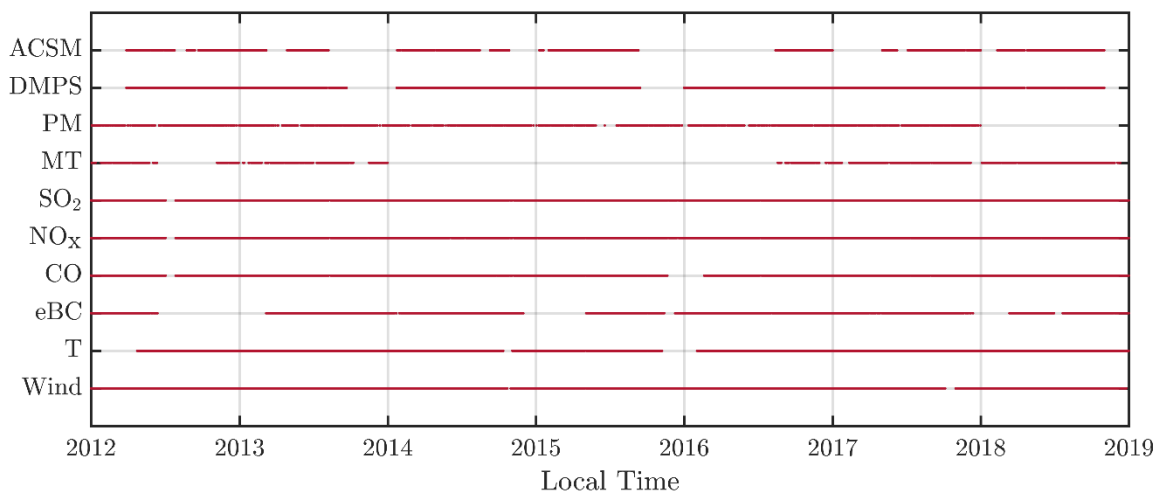
1224

1225



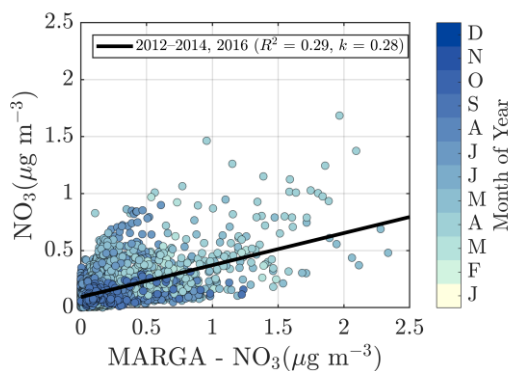
1227

1228 **Figure A.1** Wind rose diagrams during the overall measurement period (panel a), February (panel b), and July (panel c). The distance
 1229 from origin reflects the likelihood of each direction (%) and the color scale reflects the likelihoods of different wind speeds associated
 1230 with the direction.



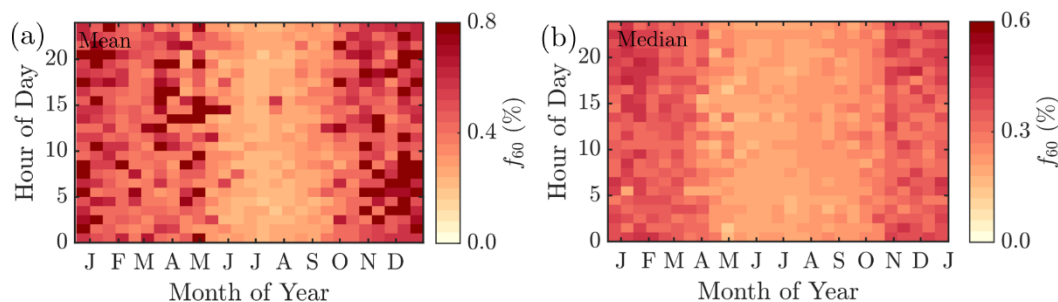
1231

1232 **Figure A.2** Data availability during the measurement period. The instrument/measurement parameter is on the y-axis and time is on
 1233 the x-axis. Gaps in the red line correspond to times when no data was available.



1234

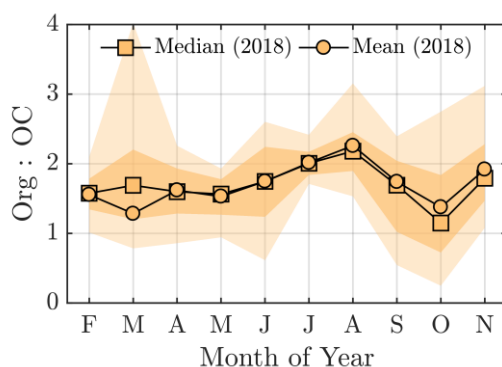
1235 **Figure A.3** The ACSM nitrate vs the PM_{2.5} nitrate detected with MARGA-2S. The color coding represents the month of the year.
 1236 The black line represents the overall linear fit.



1237

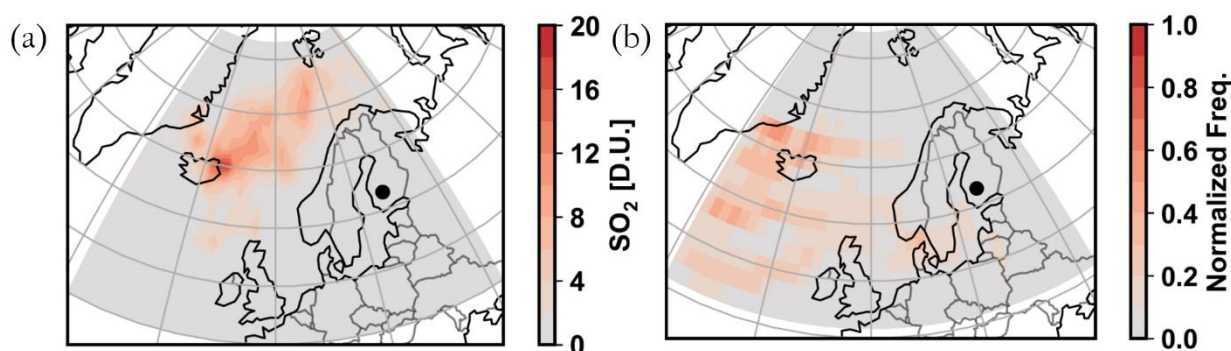
1238 **Figure A.4** The mean (a-panel) and median (b-panel) f_{60} (the fraction of m/Q 60 Th signal of the total OA signal) values derived from
 1239 the ACSM measurements (2012–2018 at SMEAR II). The x-axes represent the time of the year and the y-axes the hour of the day
 1240 (UTC+2). The coloured pixels represent the f_{60} values. Note the different colour scales between the mean and median figures. It is also
 1241 worth mentioning that due to the rather low signal to noise ratio of the ACSM, the f_{60} estimates can be very noisy. To avoid the weight
 1242 of the high and low noise extremes in the a-panel (mean f_{60}), only the range of $0 \leq f_{60} \leq 1$ were included in the f_{60} mean field calculation.

1243



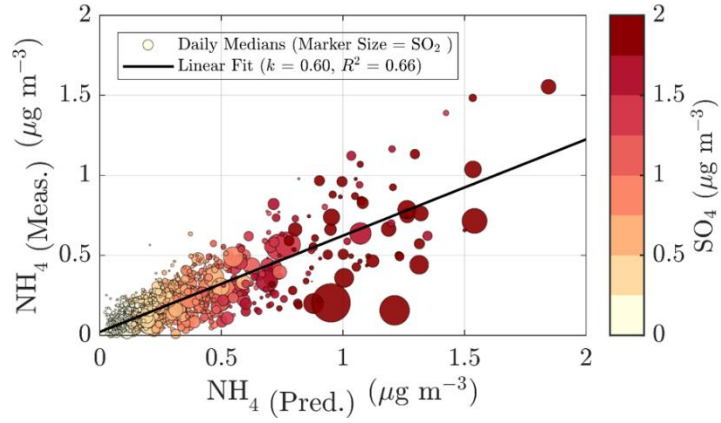
1244

1245 **Figure A.5** Organic carbon concentration (OC) vs the organic aerosol concentration (Org) in 2018 at SMEAR II. The darker yellow
 1246 shadings indicate the area between the 25th and 75th percentiles and the lighter yellow the area between the 10th and 90th percentiles.



1247

1248 **Figure A.6** (Panel a) Average SO_2 concentration in the atmospheric column derived from the ozone monitoring instrument (OMI)
 1249 aboard Aura satellite for September 2014. High values near Iceland are due to the 2014–2015 flood lava eruption of the Bárðarbunga
 1250 volcano. (Panel b) 2D normalized histogram of air parcel back trajectories arriving at the SMEAR II station for September 2014. The
 1251 trajectories are computed using the HYSPLIT model going back 96 hours in time with a resolution of 9 arriving trajectories per hour.
 1252 Each air parcel path is recorded for each hour. These points are binned in 2×2 degree cells. The counting of each cell is then normalized
 1253 by multiplying it with the square of the distance to the SMEAR II station (black disk marker) in order to highlight the long-range
 1254 transport patterns.



1255

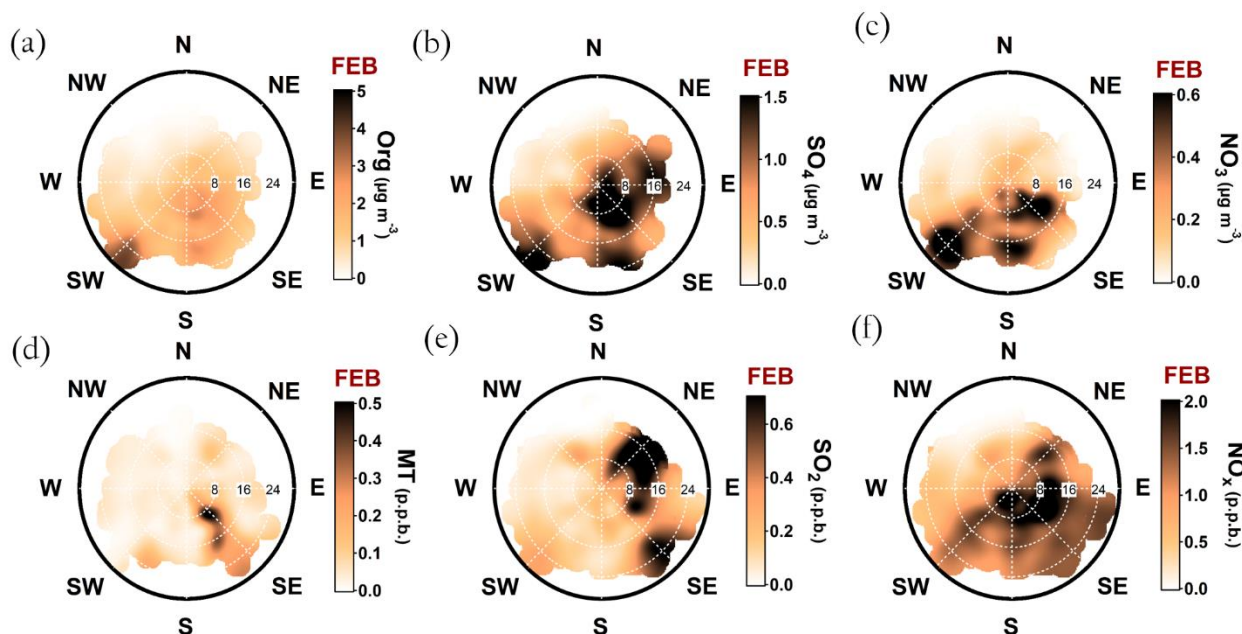
1256

1257

1258

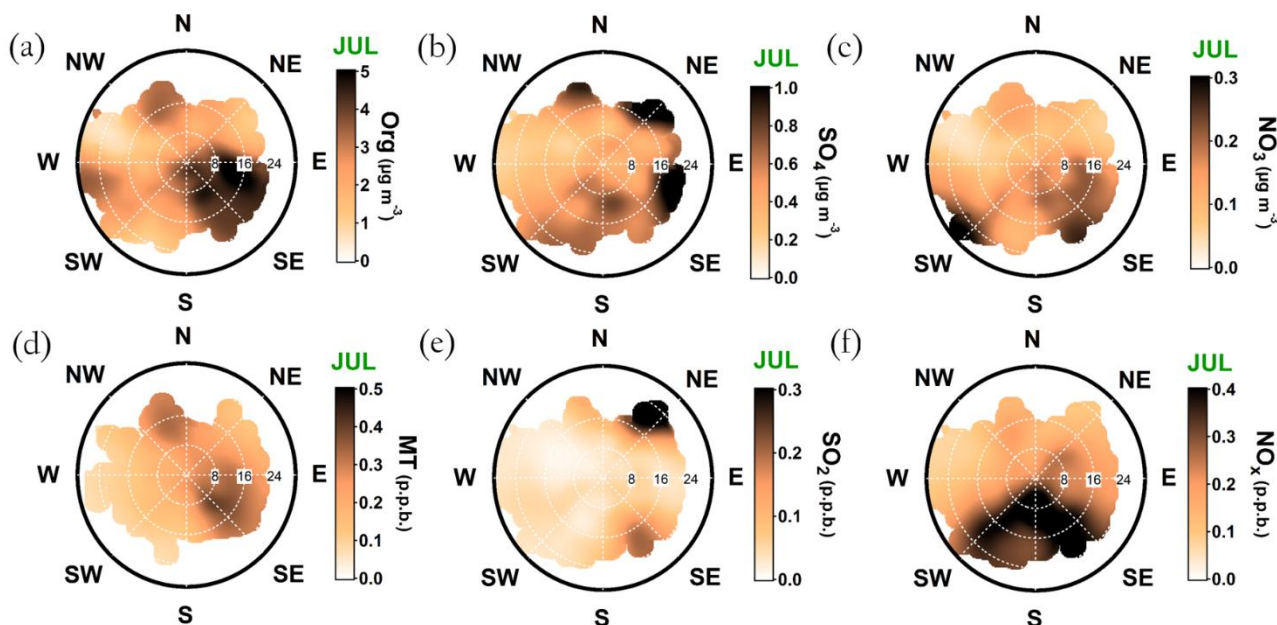
1259

Figure A.7 The relationship between the measured and predicted ammonium concentrations. The marker size reflects the ambient SO_2 concentration and the colour scale sulphate concentration. The linear fit represents the ratio between the measured and predicted ammonium concentration. Drifting from 1 could be linked to more basic or acidic aerosols. The linear fit of 0.66 indicates a possibility of acidic aerosols that decreases in the presence of SO_2 . A better acidity approximation could be derived with thermodynamical models.



1260

1261 **Figure A.8** Openair polar plots for organic aerosol (panel a), sulphate (panel b), nitrate (panel c), monoterpenes (panel d), SO_2 (panel
 1262 e), and NO_x (panel f) during February. The distances from the origin indicates wind speeds in km h^{-1} . The wind speed grid lines are
 1263 presented with white dashed circles. The colour scales represent the concentrations observed with each wind speed and direction
 1264 combinations. As the figures do not indicate any likelihood of the wind speed and distance combinations, [Figure A.1](#) is important to
 1265 keep in mind while interpreting them. Briefly, N–NE–E is the least probable wind direction, whereas S–SW–W is the most likely.
 1266 Wind speeds generally stay below 20 km h^{-1} .



1267

1268 **Figure A.9** Openair polar plots for organic aerosol (panel a), sulphate (panel b), nitrate (panel c), monoterpenes (panel d), SO_2 (panel
 1269 e), and NO_x (panel f) during July. The distances from the origin indicates wind speeds in km h^{-1} . The wind speed grid lines are
 1270 presented with white dashed circles. The colour scales represent the concentrations observed with each wind speed and direction
 1271 combinations. As the figures do not indicate any likelihood of the wind speed and distance combinations, [Figure A.1](#) is important to
 1272 keep in mind while interpreting them. Briefly, N–NE–E is the least probable wind direction, whereas S–SW–W is the most likely. Wind speeds
 1273 generally stay below 20 km h^{-1} .